



## Report Title

Synchrotron White Beam X-ray Topography of LGX and SXGS Bulk Single Crystals, Thin Films and Piezoelectric Devices

### ABSTRACT

This project comprised a program of research aimed at applying the technique of Synchrotron White Beam X-ray Topography (SWBXT), supplemented by the complementary technique of High Resolution Triple-Axis X-ray Diffraction (HRTXD), to the determination of defect and general distortion distributions in novel LGX piezoelectric crystals with a view to enabling improvement in crystal quality and consequently in piezoelectric device performance. The LGX family of compounds, which includes langasite, LGS (La<sub>3</sub>Ga<sub>5</sub>SiO<sub>14</sub>), and its isomorphs, langanite or LGN (La<sub>3</sub>Ga<sub>5.5</sub>Nb<sub>0.5</sub>O<sub>14</sub>) and langatate or LGT (La<sub>3</sub>Ga<sub>5.5</sub>Ta<sub>0.5</sub>O<sub>14</sub>), as well as several other variants, are of current interest for application as bulk wave resonators for precision oscillators, with all these materials exhibiting high piezoelectric coupling, low acoustic loss (high Q) and temperature compensation. However, the influence of crystal quality on piezoelectric properties, for example, on mode shapes dictates that high quality crystals are required for this technology to reach full potential. This requires collaboration between crystal growers and characterizers to gain an understanding of the defect content of the crystals and to enable optimization of growth parameters.

To this end, detailed SWBXT studies will be carried out on:

- (1) bulk LGX crystals grown using the Czochralski technique,
- (2) homo- and heteroepitaxial thin films of LGX, and
- (3) various LGX resonator structures including Surface Acoustic Wave (SAW) resonators.
- (4) Selected Quartz Resonators
- (5) SiC substrates/epilayers

---

### List of papers submitted or published that acknowledge ARO support during this reporting period. List the papers, including journal references, in the following categories:

#### (a) Papers published in peer-reviewed journals (N/A for none)

1. J. Luo, D. Shah, C.F. Klemenz, M. Dudley and H. Chen, "The Czochralski Growth of Large Diameter La<sub>3</sub>Ga<sub>5.5</sub>Ta<sub>0.5</sub>O<sub>14</sub> Crystals Along Different Orientations", J Cryst. Growth, 287, 300-304, (2006).
2. G. Dhanaraj, M. Dudley, Y. Chen, B. Ragothamachar, B. Wu and H. Zhang, "Epitaxial Growth and Characterization of Silicon Carbide Films", J Cryst. Growth, 287, 344-348, (2006).
3. B. Ragothamachar, G. Dhanaraj, J. Bai and M. Dudley, "Defect Analysis in Crystals using X-ray Topography," Microscopy Research and Technique, 69, 343-358, (2006) (Invited Paper).
4. M. Dudley, J. Bai, X. Huang, W.M. Vetter, G. Dhanaraj and B. Ragothamachar "Synchrotron White Beam X-ray Topography, Transmission Electron Microscopy and High Resolution X-ray Diffraction Studies of Defects and Strain Relaxation Processes in Wide Bandgap Semiconductor Crystals and Thin Films", Mater. Science in Semicon. Process., 9, 315-322, (2006).
5. G. Dhanaraj, Y. Chen, H. Chen, D. Cai, H. Zhang, and M. Dudley, "Chemical Vapor Deposition of Silicon Carbide Epitaxial Films and Their Defect Characterization", J. Electron. Mater., 35, 1513-1517, (2007).

Number of Papers published in peer-reviewed journals: 5.00

---

#### (b) Papers published in non-peer-reviewed journals or in conference proceedings (N/A for none)

Number of Papers published in non peer-reviewed journals: 0.00

---

#### (c) Presentations

Number of Presentations: 0.00

---

#### Non Peer-Reviewed Conference Proceeding publications (other than abstracts):

---

**Peer-Reviewed Conference Proceeding publications (other than abstracts):**

1. M. Dudley, X.R. Huang, W.M. Vetter, and G. Dhanaraj, "Synchrotron White Beam X-ray Topography Characterization of Defects in Technologically Important SiC and InP Single Crystals", in "Crystal Growth and Characterization: Proceedings of International Workshop on the Preparation and Characterization of Technologically Important Single Crystals", S.K. Gupta, S.K. Halder, and G. Bhagavannarayana (Eds.), National Physical Laboratory New Delhi, Feb. 26-28, 2001, pp. 44-51, (2001).
2. M. Dudley, B. Raghathamachar, H. Chen, A.J. Khan, S. Tiddrow, and C. Fazi, "Characterization of Defect and Strain Configurations in Langanite and Langatate Single Crystals using Synchrotron White Beam X-ray Topography and Assessment of their Influence on Resonator Performance" in Proceedings of 14th European Frequency and Time Forum, Turin Italy, March 14-16, 2000, (2001).
3. M. Dudley, B. Raghathamachar, H. Chen, W. Johnson, S. Tiddrow, A. Khan, and C. Fazi, "Diagnostic Synchrotron Topographic Imaging of Striations and other Defects in Langatate and Langanite Single Crystals and Assessment of their Influence on Resonator Performance" in Proceedings of 15th European Frequency and Time Forum, Neuchatel, Switzerland, March 6-8, 2001, FSRM (Swiss Foundation for Research in Microtechnology), Neuchatel, Switzerland, (2001), pp.284-288.
4. Y. Chen, G. Dhanaraj, H. Chen, W. Vetter, M. Dudley, and H. Zhang, "Chemical Vapor Deposition and Defect Characterization of Silicon Carbide Epitaxial Films" in "Progress in Semiconductor Materials V - Novel Materials and Electronic and Optoelectronic Applications, L.J. Olafsen, A. Saxler, M.C. Wanke, and R.M. Biefeld (Eds.), Mater. Res. Soc. Symp. Proc., 891, EE12-11.1-EE12-11.6, (2006).
5. G. Dhanaraj, Y. Chen, H. Chen, H. Zhang, and M. Dudley, "Growth Mechanism and Dislocation Characterization of Silicon Carbide Epitaxial Films", in "Silicon Carbide – Materials, Processing, and Devices", M. Dudley, M.A. Capano, T. Kimoto, and A.R. Powell, and S. Wang (Eds.), Mater. Res. Soc. Symp. Proc., 911, 0911-B05-27, 157-162, Warrendale, PA, (2006).
6. H. Chen, G. Wang, Y. Chen, X. Jia, J. Bai, and M. Dudley, "The Formation Mechanism of Carrot Defects in SiC Epifilms", in "Silicon Carbide – Materials, Processing, and Devices", M. Dudley, M.A. Capano, T. Kimoto, and A.R. Powell, and S. Wang (Eds.), Mater. Res. Soc. Symp. Proc., 911, 0911-B05-24, 163-168, Warrendale, PA, (2006).
7. H. Chen, B. Raghathamachar, W. Vetter, M. Dudley, Y. Wang, B.J. Skromme, "Effects of Different Defect Types On the Performance of Devices Fabricated On a 4H-SiC Homoepitaxial Layer", in "Silicon Carbide – Materials, Processing, and Devices", M. Dudley, M.A. Capano, T. Kimoto, and A.R. Powell, and S. Wang (Eds.), Mater. Res. Soc. Symp. Proc., 911, 0911-B12-03, 169-174, Warrendale, PA, (2006).
8. G. Dhanaraj, Y. Chen, M. Dudley and H. Zhang, "Growth and Surface Morphologies of 6H-SiC Bulk and Epitaxial Crystals", in Silicon Carbide and Related Materials 2005, Materials Science Forum, 527-529, 67-70, R.P. Devaty, D.J. Larkin, and S. Sadow (Eds.), Trans Tech Publications, Switzerland, (2006).
9. Y. Chen, H. Chen, N. Zhang, M. Dudley, and R. Ma, "Investigation and of Low Angle Grain Boundaries in Hexagonal Silicon Carbide", to appear in "Advances in III-V Nitride Semiconductor Materials and Devices", C.R. Abernathy, H. Jiang, and J.M. Zavada (Eds.), Mater. Res. Soc. Symp. Proc., 955E, 0955-107-50 (6 pages), Warrendale, PA, (2007)

**Number of Peer-Reviewed Conference Proceeding publications (other than abstracts):**

9

---

**(d) Manuscripts****Number of Manuscripts:** 0.00

---

**Number of Inventions:**

---

**Graduate Students**

<u>NAME</u>	<u>PERCENT SUPPORTED</u>
Huaibin Chen	1.00
Jie Bai	0.10
Yi Chen	0.10
Hui Chen	0.10
<b>FTE Equivalent:</b>	<b>1.30</b>
<b>Total Number:</b>	<b>4</b>

**Names of Post Doctorates**

<u>NAME</u>	<u>PERCENT SUPPORTED</u>
Govindhan Dhanaraj	0.10
<b>FTE Equivalent:</b>	<b>0.10</b>
<b>Total Number:</b>	<b>1</b>

**Names of Faculty Supported**

<u>NAME</u>	<u>PERCENT SUPPORTED</u>	National Academy Member
Michael Dudley	0.25	No
<b>FTE Equivalent:</b>	<b>0.25</b>	
<b>Total Number:</b>	<b>1</b>	

**Names of Under Graduate students supported**

<u>NAME</u>	<u>PERCENT SUPPORTED</u>
<b>FTE Equivalent:</b>	
<b>Total Number:</b>	

**Student Metrics**

This section only applies to graduating undergraduates supported by this agreement in this reporting period

The number of undergraduates funded by this agreement who graduated during this period: .....

The number of undergraduates funded by this agreement who graduated during this period with a degree in science, mathematics, engineering, or technology fields:.....

The number of undergraduates funded by your agreement who graduated during this period and will continue to pursue a graduate or Ph.D. degree in science, mathematics, engineering, or technology fields:.....

Number of graduating undergraduates who achieved a 3.5 GPA to 4.0 (4.0 max scale):.....

Number of graduating undergraduates funded by a DoD funded Center of Excellence grant for Education, Research and Engineering:.....

The number of undergraduates funded by your agreement who graduated during this period and intend to work for the Department of Defense .....

The number of undergraduates funded by your agreement who graduated during this period and will receive scholarships or fellowships for further studies in science, mathematics, engineering or technology fields:.....

**Names of Personnel receiving masters degrees**

<u>NAME</u>	
Huaibin Chen	
Jie Bai	
Yi Chen	
Hui Chen	
<b>Total Number:</b>	<b>4</b>

---

**Names of personnel receiving PhDs**

NAME

Huaibin Chen

Jie Bai

**Total Number:**

2

---

**Names of other research staff**

NAME

PERCENT SUPPORTED

**FTE Equivalent:**

**Total Number:**

---

**Sub Contractors (DD882)**

**Inventions (DD882)**

## **Foreword**

This document is the final report of a project funded through Dr. Chris Fazi at Army Research Laboratory (ARL) via Dr. John Prater at Army Research Office. It involved examination of the defect and strain content in the novel piezoelectric crystal langasite, its polymorphs and other related piezoelectric materials. Defect and strain microstructure is known to exert significant negative influence on piezoelectric device performance so that analysis of the origins of the defects and strains can be used to facilitate the development of strategies aimed at mitigating these deleterious effects. To this end the technique of Synchrotron White Beam X-ray Topography (SWBXT) was used to elucidate the defect and strain microstructure in these materials. Such information could then be fed back to the crystal growers in order to suggest strategies for intelligent manipulation of crystal growth parameters to suitably modify the defect microstructure. In the final year of this project, supplemental funds were provided by Dr. Ken Jones at ARL to examine the correlation between substrate and epilayer defect structures in 4H-SiC homoepitaxial layers. Results from this are included in the final section of this report.

## Table of Contents

List of Illustrations and Tables .....	3
Statement of the problem studied .....	4
Summary of the most important results .....	6
LGX and Related Materials .....	6
Topography of LGX and Related Boules .....	6
LGT and LGN Boules.....	6
LGS Boules.....	10
STGS Boule .....	22
Topography of LGX and Related Wafers.....	25
Expected Geometry of Striations in LGX Wafers .....	25
LGN Wafers.....	27
LGT Wafers .....	29
CTGS Wafers.....	31
Topography of LGX Resonators.....	33
Discussion: Origins of Striations in LGX and Related Crystals and Strategies for their Avoidance.....	34
Discussion: Assessing the Influence of Striations .....	35
Quartz.....	35
Study of Quartz Crystal Bar.....	35
Study of Quartz Crystal Wafers.....	38
Study of Quartz Resonators .....	42
Discussion of the Quartz Crystal Studies.....	51
Silicon Carbide.....	52
Plan-view SWBXT study of replication/dissociation of MPs after epilayer growth	52
Cross-sectional SWBXT study of CVD grown epitaxial layers.....	53
Computer modeling of the SWBXT images of MP after dissociation into 1c TSD cluster.....	54
TEM study of MP dissociation after n <sup>-</sup> drift layer growth.....	55

## List of Illustrations and Tables

Figure 1. Back reflection geometry .....	6
Figure 2. Schematic Diagram of Reflection Geometry .....	7
Figure 3. The tail end of the boule with the relative rotation angle positions .....	7
Figure 4. SWBXT images recorded from 00-A1-08 LGT-X boule.....	9
Figure 5. Enlargement of topograph II-(b) showing striations, K, precipitates, P, wavy surface feature, A, and rough surface feature C.....	9
Figure 6. Enlargement of topograph III-(b) showing striation, K, precipitates, P, and facets, F. In this case, striations are clearly shown in the facets.....	9
Figure 7. Enlargement of a topograph from 01-A4-07 LGN boule showing well-defined striations, K, precipitates, P, and wavy surface features, A. White bands, C, are due to heavy surface ridges.....	10
Figure 8. Enlargement of a topograph from 00-A4-17 LGT boule showing that the wavy surface features, A, are superimposed on the well-defined striations contrast, K.....	10
Figure 9. Enlargement of a topograph from 00-A4-17 LGT boule, risers on facet steps (with the (0001) orientation) block the diffracted beam thereby causing bands of white contrast F. The smooth surface of the facet produces good striation image K.....	10
Figure 10. Schematic Diagram of Reflection Geometry .....	11
Figure 11. Tail end of the LGS-8 boule with the relative topographs sections .....	12
Figure 12. SWBXT images recorded from LGS-8 - Section A.....	14
Figure 13. SWBXT images recorded from LGS-8 - Section B .....	15
Figure 14. SWBXT images recorded from LGS-8 - Section C .....	16
Figure 15. SWBXT images recorded from LGS-8 - Section D.....	17
Figure 16. SWBXT images recorded from LGS-8 - Section E .....	18
Figure 17. SWBXT images recorded from LGS-8 - Section F.....	19
Figure 18. SWBXT images recorded from LGS-8 - Section G.....	20
Figure 19. SWBXT images recorded from LGS-8 - Section H.....	21
Figure 20. Enlarged 2-52 topograph showing precipitates, dislocations and facets.....	22
Figure 21. Inconsistent crystal growth near seed end.....	22
Figure 22. The tail and seed end of the STGS boule with the relative rotation angle positions.....	23
Figure 23. SWBXT images recorded from STGS boule .....	24
Figure 24. Enlargement of topograph (i) in 90° ~ 180° quadrant showing wavy surface feature, A, and vertical white contrast facet features, F, along with some striation-like contrast.....	24
Figure 25. A possible configuration of interface shape/growth striations in LGX crystals .....	25
Figure 26. Transmission topographs recorded from two LGX wafers with $g = 0002$ .....	26
Figure 27. Enlargement of the core region and the surrounding slip bands .....	27
Figure 31. Optical micrograph showing central core region and facets .....	29
Figure 32. Topograph recorded from Z-cut plate of LGT. Note the straight striation images, K, indicative of faceting. C indicates cracks, D dislocations .....	29
Figure 33. Discontinuous growth on the (10-10) and (1-100) facet planes leads to facet formation.....	30

Figure 35. Transmission topographs recorded from LGN resonators .....	34
Figure 36. Topographs of quartz bar +X surface.....	36
Figure 37. Topographs of quartz bar -X surface.....	36
Figure 38. Paired subgrains on +/-X surfaces.....	37
Figure 39. Topographs of quartz bar -Z surface .....	37
Figure 40. Topographs of quartz bar +Z surface .....	37
Figure 41. Dislocations on -Z surface parallel to X direction.....	38
Figure 44. Photographs of quartz resonator A.....	42
Figure 45. Transmission topographs of quartz resonator A.....	43
Figure 46. Photographs of quartz resonator B .....	44
Figure 47. Transmission topographs of quartz resonator B.....	45
Figure 48. Photographs and transmission topographs of quartz resonator C .....	46
Figure 49. Photographs of quartz resonator D .....	47
Figure 50. Transmission topographs of quartz resonator D.....	47
Figure 51. Photographs of quartz resonator E .....	48
Figure 52. Transmission topographs of quartz resonator E .....	49
Figure 53. Photographs of quartz resonator F.....	50
Figure 54. Transmission topographs of quartz resonator F .....	50
Figure 55. Comparison of (11-28) grazing-incidence SWBXT image before (left) and after (right) epilayer growth. The MPs are clearly modified.....	52
Figure 56. Cross sectional SWBXT of SiC wafer after epilayer growth showing the conversion of BPDs into TEDs during CVD growth. The total thickness is ~430 $\mu$ m. ....	53
Figure 57. Optical images showing the dissociation of MPs into closed-core TSDs. Left: KOH etch pattern on the epilayer surface; middle: cross sectional view of closing of MP at the substrate-epilayer interface; right: MP from the back side (C-face) of the wafer. .	53
Figure 58. Cross-sectional image showing the closing of MP at the interface between substrate and epilayer (left) and its (0004) transmission SWBXT (right). Sample thickness: ~430 $\mu$ m. ....	54
Figure 59. Ray-tracing simulated images of dissociated 1c TSD cluster. The simulated image elementary TSD cluster which consists of n number of 1c TSDs appears as the same configuration as a MP with Burgers vector nc. ....	54
Figure 60. (1-100) dark field image of a closed-core TSD present in the etch pit (left). It is probably dissociated from the MP during CVD growth. Multibeam image at higher magnification (right), showing the tilted TSD running through the sample.....	55

## Statement of the problem studied

Recent research, conducted in Russia, France, Japan, Germany, Ukraine, South Korea and United States, has shown that langasite ( $\text{La}_3\text{Ga}_5\text{SiO}_{14}$  or LGS) and its two isomorphs langanite ( $\text{La}_3\text{Ga}_{5.5}\text{Nb}_{0.5}\text{O}_{14}$  or LGN) and langatate ( $\text{La}_3\text{Ga}_{5.5}\text{Ta}_{0.5}\text{O}_{14}$  or LGT) (collectively referred to as LGX) with the  $\text{Ga}_3\text{Ga}_2\text{Ge}_4\text{O}_{14}$ -type structure exhibit promising piezoelectric properties intermediate between those of quartz and  $\text{LiNaO}_3$  and  $\text{LiTaO}_3$ .

They have temperature compensation at near room temperature, high frequency stability and adequate electromechanical coupling factors for both SAW and BAW devices. Moreover, they also showed that these crystals have very low acoustic friction, which indicates high Q factor. The combination of all these properties, with their high phase transformation temperature and the availability of high quality crystals, makes these crystals currently the most promising piezoelectric materials and useful for a lot of application not only under room temperature but also under high temperature conditions.

It is commonly acknowledged that the performance, yield, reliability and degradation of piezoelectric devices, are largely determined by the compositional homogeneity and the presence of defects of the crystals, which the devices are made from. For example, the influence of defects and strain on the modification of mode shapes dictates that high quality crystals are required for this technology to reach full potential. Therefore, in order to gain the sufficiently "perfect" crystals, it is imperative to understand the mechanism of defect generation during crystal growth. Such understanding must be based on the detailed information on the nature and distribution of imperfections in as-grown crystals. Thus, characterization of structural and compositional perfection of the crystal grown is critical to improve the quality and performance of electric devices.

As part of the research program, some specifically emphasized issues to be directly addressed involving all langasite structure compounds, through the development of experiments and theory, include:

- Identification, and development of maps of all of the defects and strains present in crystals of LGS, LGN, LGT and other "ordered" langasite structure crystals grown by various manufacturers;
- Determination of the influence of the various types of defects and strains present in resonators manufactured from the various crystals;
- Provide detailed information on the relationship between growth parameters and defect microstructure.

Results obtained in this research program are likely to provide useful information on the relationship between observed growth defects and growth parameters in these potential resonator crystals and should enable strategy development for crystals' and resonators' quality and performance improvement. Detailed information will also be possibly able to reveal the influence on resonator performance of the various kinds of defect present in the different crystals.

In previous reports we provided a preliminary survey of the quality of langasite, langanite and langatate crystals carried out using SWBXT. Here we report the results of a more systematic study of the defects and strain configuration of LGX crystal boules, wafers and resonators. This enables some insight to be gained as to the evolution of the three-dimensional defect microstructure, including the interface shape, during growth.

Data have been obtained from all types of crystals. A selection from these is presented below, following the fabrication procedure of LGX crystal devices, i.e., from as-grown LGX crystal boules to crystal wafers cut from adjacent locations in the LGX boule to resonators made from the wafers.

Preliminary results on the defects content of newly developed “ordered” langasite structure compound STGS and CTGS are also presented here.

Due to the currently common use of quartz as a piezoelectric material, a parallel investigation of raw quartz crystals and its resonators was also carried out.

Results from an investigation of defect propagation from substrate to epilayer in 4H-SiC homoepitaxy carried out in the final year of this project are included at the end of this report.

## Summary of the most important results

### *LGX and Related Materials*

#### Topography of LGX and Related Boules

##### LGT and LGN Boules

First, LGT and LGN boules were examined by SWBXT in back reflection geometry in order to determine the orientation. Back reflection Laue patterns were recorded. The growth axis of the boules was set to parallel to the incident beam. The diffraction geometry is shown in Fig. 1.

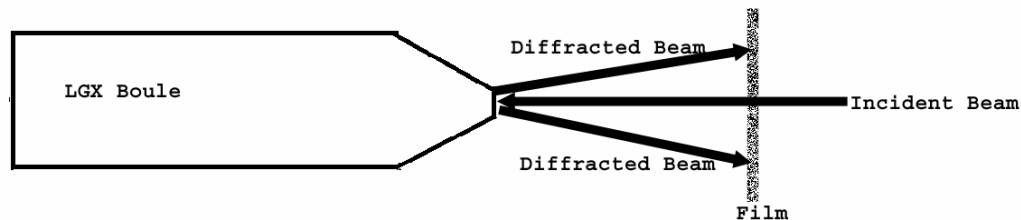


Figure 1. Back reflection geometry

The curved surface of four LGX boules, 00-A1-07 LGT-X, 00-A1-08 LGT-X, 01-A4-07 LGN and 00-A4-17 LGT were examined by SWBXT with reflection geometry, shown in Fig. 2.

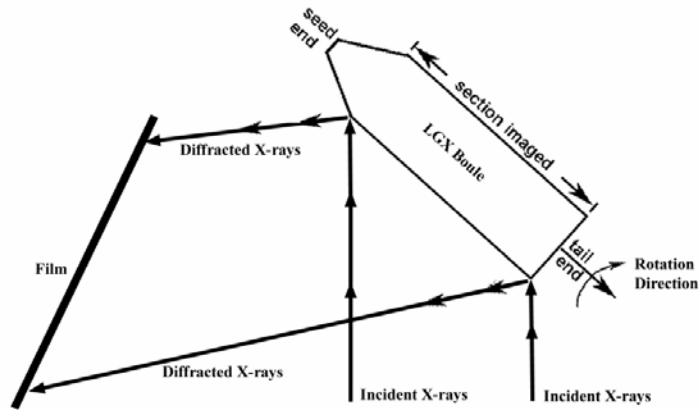


Figure 2. Schematic Diagram of Reflection Geometry

Topographs were recorded covering the entire length of the boules in longitudinal strips. Only the cylindrical surface with the roughly constant diameter was imaged. After imaging of one strip of surface, the boules were rotated by a few degrees in a clockwise direction (looking at the tail end), the next strip of surface was imaged and the topograph was recorded, until a series of topographs were recorded covering the entire cylindrical surface of the boule. The sequences of topographs are more or less continuous. The diffraction vector  $\mathbf{g}$  of each topograph is different with each other, while for all the topographs,  $\mathbf{g}$  vector is approximately pointing axially from the seed end to the tail end, i.e. from left to right on all the topographs shown in here. Results with boule 00-A1-08 LGT-X are presented and discussed here in detail.

Total of 36 topographs of the longitudinal surface of 00-A1-08 LGT-X boule were recorded with the method described above. The topographs are recorded starting from  $0^\circ$  (see Fig. 3 and the downward pointing arrow on the optical micrograph, which accompanies each group of topographs), going around the boule as the boule is rotated clockwise.

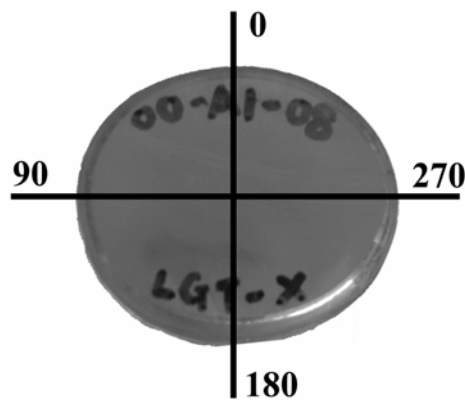
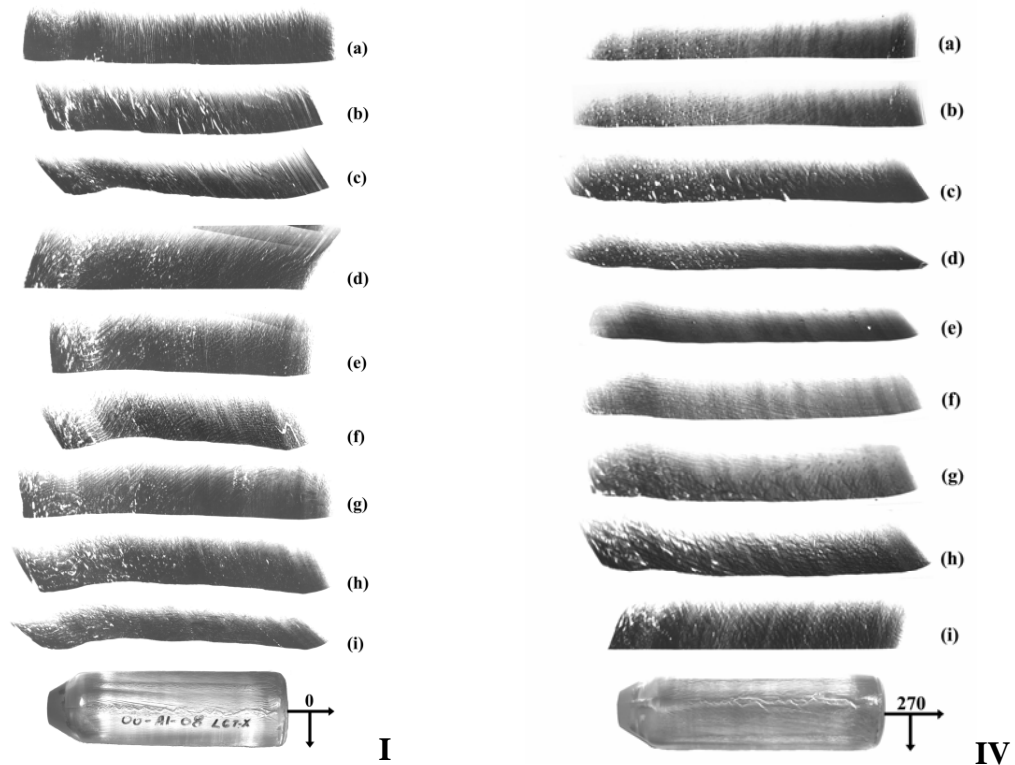


Figure 3. The tail end of the boule with the relative rotation angle positions

Each group, comprising 9 topographs, covers an approximately  $90^\circ$  curved section of the surface of the boule. Topographs were presented in four groups with respect to the corresponding optical micrograph of the boule shown at the bottom of each group of

topographs, Fig. 4. Fig. 5 shows an enlargement of topograph II-(b) in the  $90^\circ \sim 180^\circ$  quadrant. And Fig. 6 shows an enlargement of topography III-(b) in the  $180^\circ \sim 270^\circ$  quadrant.

- (1) Topographs show well-defined striations K perpendicular to the growth axis X.
- (2) Wavy contrast features A are caused by surface ridges running along the length of the boule. These are superimposed onto the striation images (also see I-(e) and I-(f) in  $0^\circ \sim 90^\circ$  quadrant).
- (3) Regions of white contrast at the tail end are probably due to the presence of precipitates, P, at the end of growth. Some precipitate type contrast is also visible in the middle sections of the boule.
- (4) The several white spots and lines in the middle of the boule, C (not precipitates P), have been created because of the presence of surface projections/depressions, such as small pits, which lead to the situation where no image is locally formed due to blockage of the diffracted beam, Fig. 5.
- (5) Vertical white contrast features F are produced in III-(a), III-(b), III-(c) and III-(d) in  $180^\circ \sim 270^\circ$  quadrant, due to risers on faceted steps on the boule (the facets have (0001) orientation) which block the diffracted beam thereby causing bands of white contrast. Where, images can be recorded from the facet itself, smooth surface produces a good quality image and for example, clear striation contrast can be observed, Fig. 6.



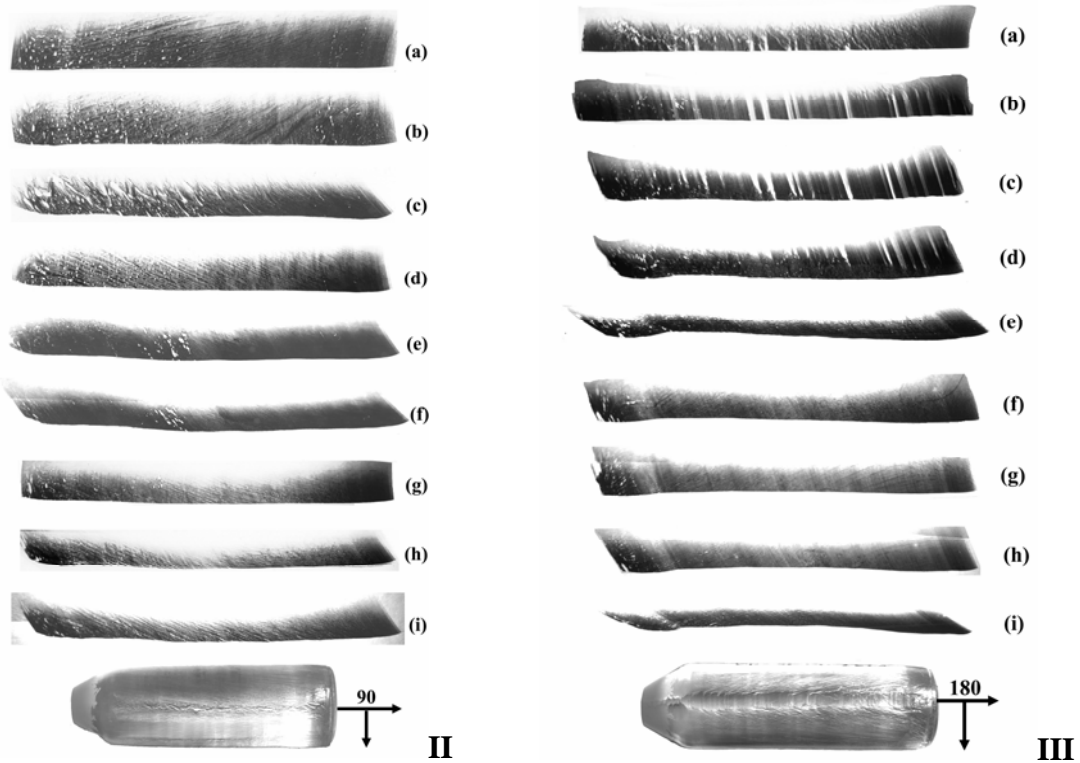


Figure 4. SWBXT images recorded from 00-A1-08 LGT-X boule

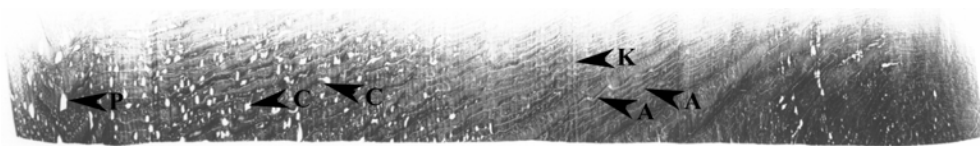


Figure 5. Enlargement of topograph II-(b) showing striations, K, precipitates, P, wavy surface feature, A, and rough surface feature C



Figure 6. Enlargement of topograph III-(b) showing striation, K, precipitates, P, and facets, F. In this case, striations are clearly shown in the facets

Some special features in the other three boules:

- (1) In boule 01-A4-07 LGN, some white contrast features running across the growth direction C are due to the heavy ridges going around the boule surface, Fig. 7.
- (2) In boule 00-A4-17 LGT, clear wavy surface features due to the ridges running across the boule are superimposed on the well-defined striation contrast, Fig. 8.
- (3) In boule 00-A4-17 LGT, vertical white contrast features F due to risers on faceted steps on the boule (the facets have (0001) orientation) which block the diffracted

beam thereby causing bands of white contrast, Fig. 9.

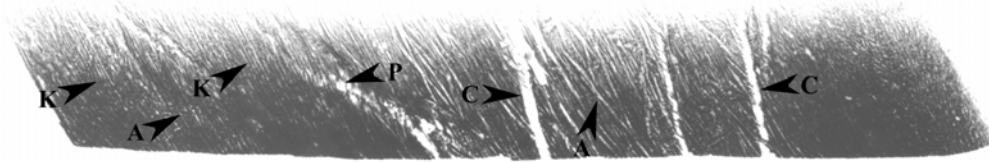


Figure 7. Enlargement of a topograph from 01-A4-07 LGN boule showing well-defined striations, K, precipitates, P, and wavy surface features, A. White bands, C, are due to heavy surface ridges

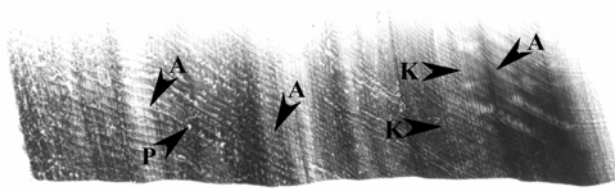


Figure 8. Enlargement of a topograph from 00-A4-17 LGT boule showing that the wavy surface features, A, are superimposed on the well-defined striations contrast, K

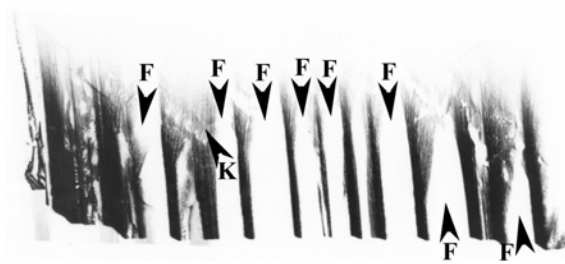


Figure 9. Enlargement of a topograph from 00-A4-17 LGT boule, risers on facet steps (with the (0001) orientation) block the diffracted beam thereby causing bands of white contrast F. The smooth surface of the facet produces good striation image K

## LGS Boules

One of the first ever commercial-size LGS single crystal boule, labeled as LGS-8, grown by Cz method was made available for studying by SWBXT. The growth direction of the boule is [0001]. The dimension of the boule is about 80mm in diameter and about 255mm in length. The cylindrical section of the boule is about 230mm long.

Near surface region of the curved surface of the crystal boule was examined by adopting X-ray topography in reflection geometry, shown in Figure 10.

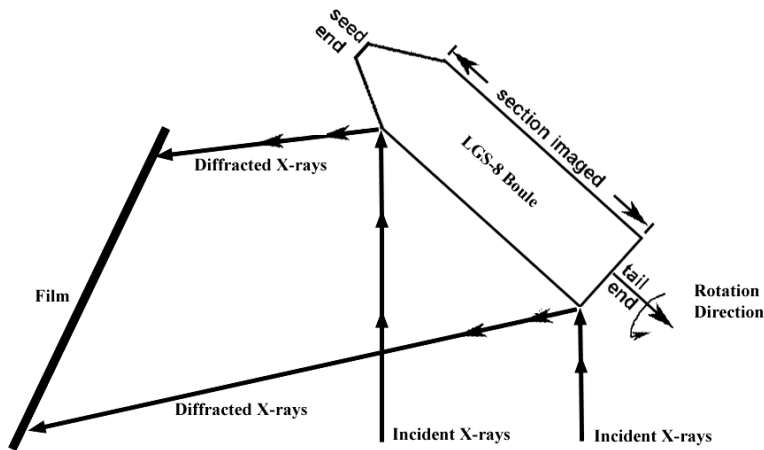


Figure 1. Schematic Diagram of Reflection Geometry

Topographs were recorded covering the entire length of the boules in longitudinal strips. The conical surface at the seed end could not be imaged. Only the cylindrical surface with the roughly constant diameter was imaged. After imaging of one strip of surface, the boule was rotated by around five degrees in a counter-clockwise direction (looking at the tail end), the next strip of surface was imaged and the topograph was recorded, until the whole surface was covered.

Due to the large size of the boule, the available synchrotron beam can not cover the whole length of the boule from tail end to seed end at the same time. Two cycles of the image recording process were conducted to image the whole surface. First set of the topographs (Group 1) cover roughly 2/3 of the length from the tail end, and another set (Group 2) roughly cover 2/3 of the length from the seed end. Thus the entire cylindrical surface of the boule was covered by total of 144 topographs.

Because of the diffraction geometry utilized, the recorded images suffer considerable distortion, especially along the length of the boule. The magnitude of distortion is different for different reflections and boule position. Accordingly, the lengths of the recorded reflection topographs vary as we rotate the boules. Still, the sequences of topographs provide an approximately continuous image of the near surface region of the boule.

The diffraction vector  $\mathbf{g}$  of each topograph is different with each other, while we rotate the boule during the whole imaging process. For all the topographs,  $\mathbf{g}$  vector is approximately pointing axially from the seed end to the tail end, i.e. from left to right on all the topographs presented here.

Topographs presented here are divided into 8 sections A to H (see Figure 11), each including two groups of 9 topographs, shown in Figure 12 to 19 accompanied by the corresponding photographs of the LGS-8 boule. Topographs labeled as 1-01 to 1-72 and 2-01 to 2-72 are started from the H-A section boundary, running clock-wise and ended at the same H-A section boundary.

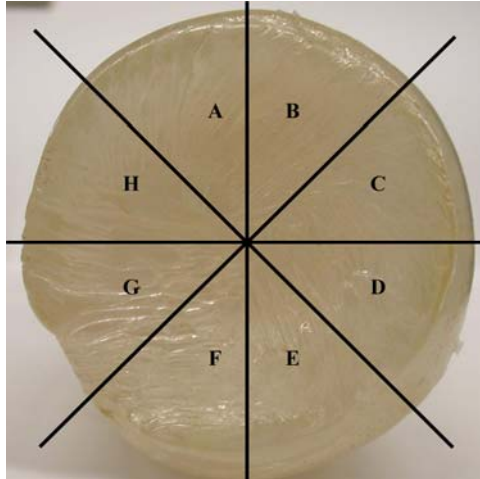


Figure 2. Tail end of the LGS-8 boule with the relative topographs sections

From micro- point of view, the available information on these topographs is very limited. The noticeable contrast features of the topographs are:

- 1) Unlike other smaller LGS, LGT and LGN boules examined and reported previously, there is no clear or well-defined striations perpendicular to the growth axis can be observed in the topographs. Although it is possible that the improvement of the growth condition and growth control thoroughly eliminated the presence of striations in the crystal, it is highly unlikely, concerning the overall growth procedure of the crystal which are discussed later in this report. It is more likely that because of the huge size of the boule, during the process of crystal growth, the temperature fluctuation, growth interface variation or chemical composition variation at the NEAR surface region were very small. Thus, the examination of the near surface region by X-ray diffraction with reflection geometry can only produce very limited information and can not reveal the true nature of the defects distribution in the crystal. Wafers cut from the boule need to be examined to completely understand the defects configuration of the crystal.
- 2) Due to the roughness of the boule surface, wavy contrast features are dominant in all the topographs. Those wavy contrast features are caused by surface ridges running in all directions throughout the whole curved surface of the crystal.
- 3) Many irregular shaped white spots and lines in the topographs are created because of the presence of surface projections/depressions, such as small pits, which lead to the situation where no image is locally formation due to blockage of the diffracted beam.
- 4) Near the seed end region, numerous white spots are evenly distributed, which are probably due to the presence of precipitates, P, at the time of the growth. Figure 20 is an enlarged image of the seed end from 2-52 topograph. Some precipitate type contrast is also visible in the middle sections of the boule.
- 5) Short ranged dislocation-like contrast can also be found around the seed end

region, shown as D in Figure 20.

- 6) Vertical white contrast features F are produced in most of the group 2 topographs (Figure 20), due to risers on faceted steps on the boule (the facets have (0001) orientation) which block the diffracted beam thereby causing bands of white contrast. Although here the images can be recorded from the facet itself, smooth surface produces a good quality image, there is still no visible striation contrast.

From macro- point of view, the continuous topographs indicates that during the crystal growth, at least two major disruptions were introduced and severely degrade the quality of the crystal (see figure 21)l.

The first disruption happened right at the end of the facet phase of the crystal. Consistent crystal growth was interrupted due to some unknown reason, and after a transition phase, crystal growth returned to normal.

The second major disruption is more obvious near the tail end of the crystal. Normal growth was interrupted again and this time even after the transition phase, part of the crystal became completely amorphous. A shift of the cylindrical axis of the crystal boule after the disruption is noticeable.

At this time, it is not clear how those inconsistent growth happened. But the X-ray topographs clearly show the degrading of the crystal quality when it happened.

The production of the first ever commercial-sized LGS crystal is a big step towards the real application of this family of promising piezoelectric crystal. But SWBXT study shows that there are problems that need to be further addressed, such as the localized dislocations and precipitates. Further examination of wafers cut from the crystal is essential to determine to quality of the crystal. More importantly, the inconsistent growth problem reveal in this study has to be investigated and resolved before the mass production become possible.

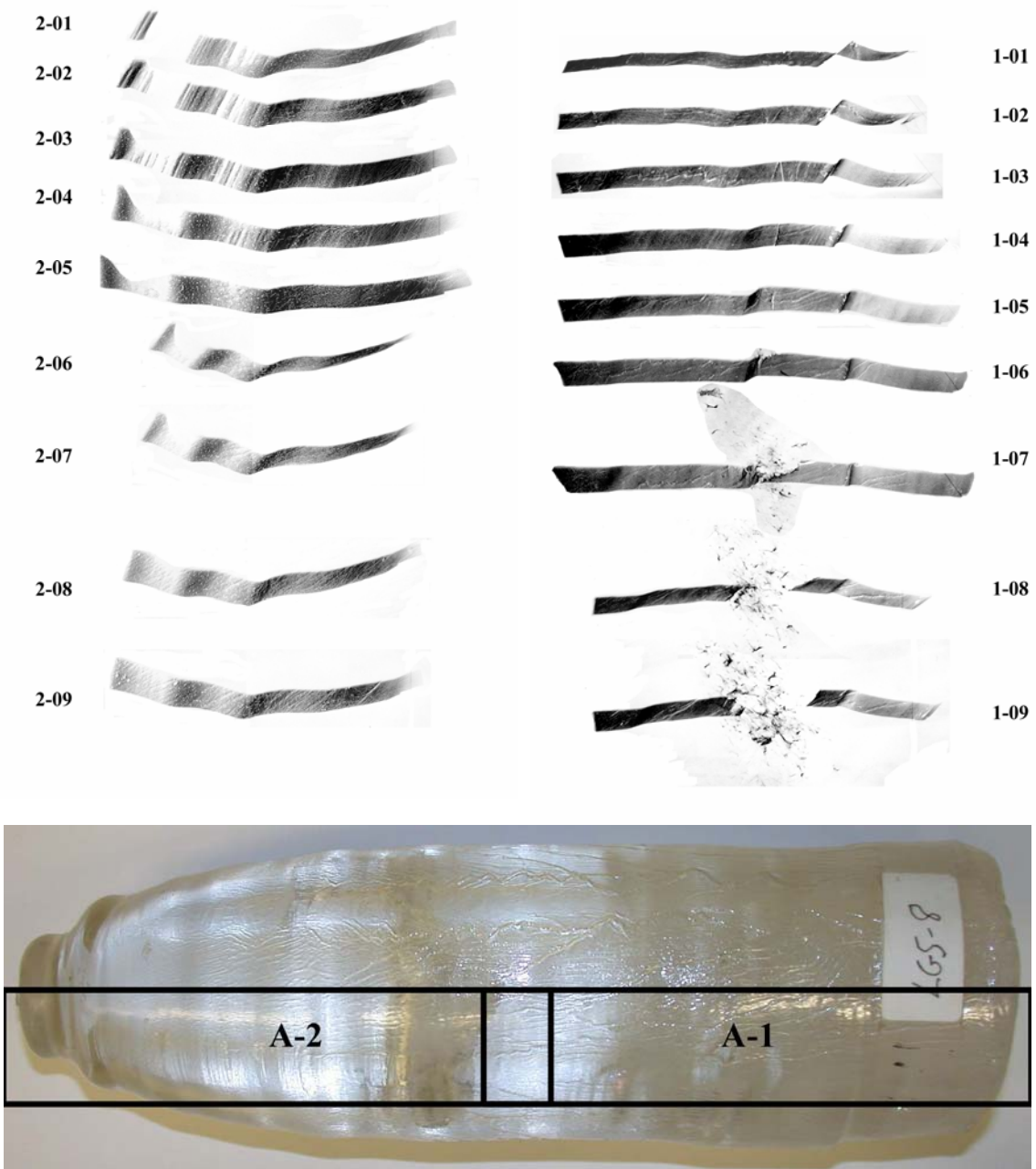


Figure 3. SWBXT images recorded from LGS-8 - Section A

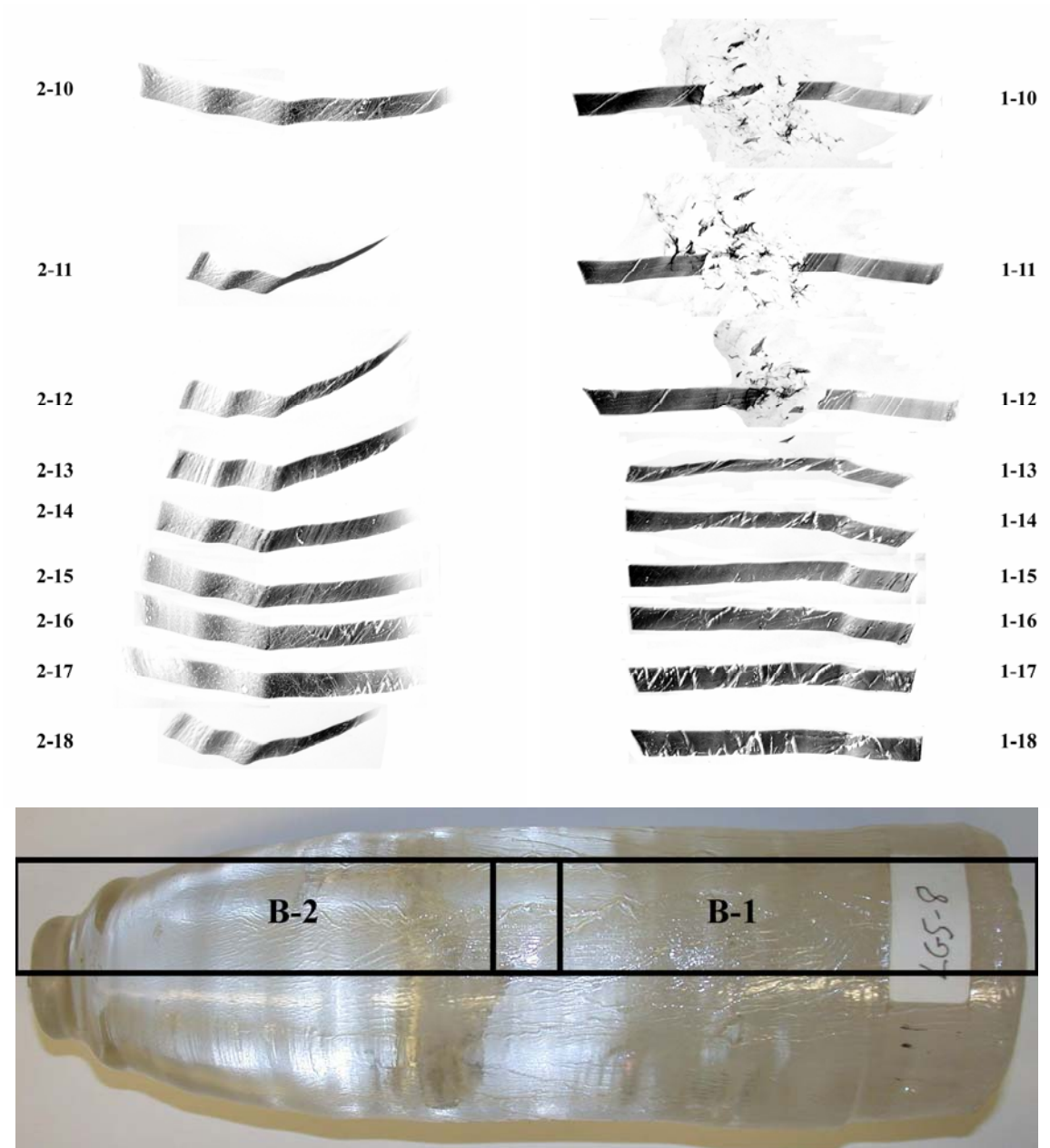


Figure 4. SWBXT images recorded from LGS-8 - Section B

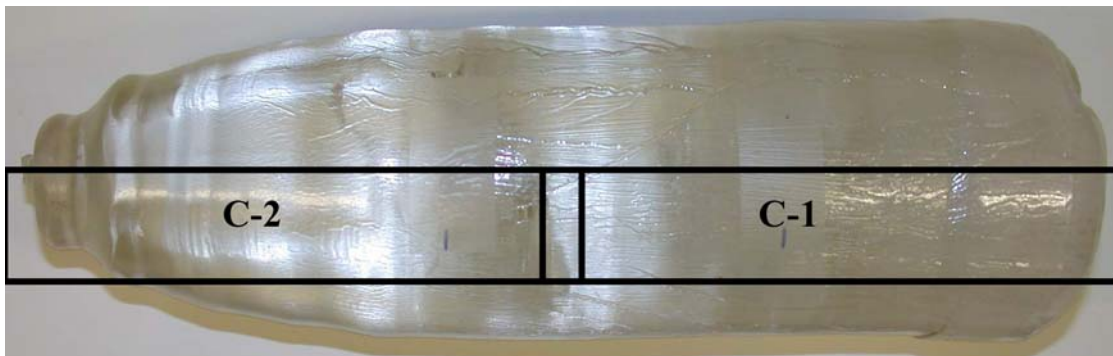
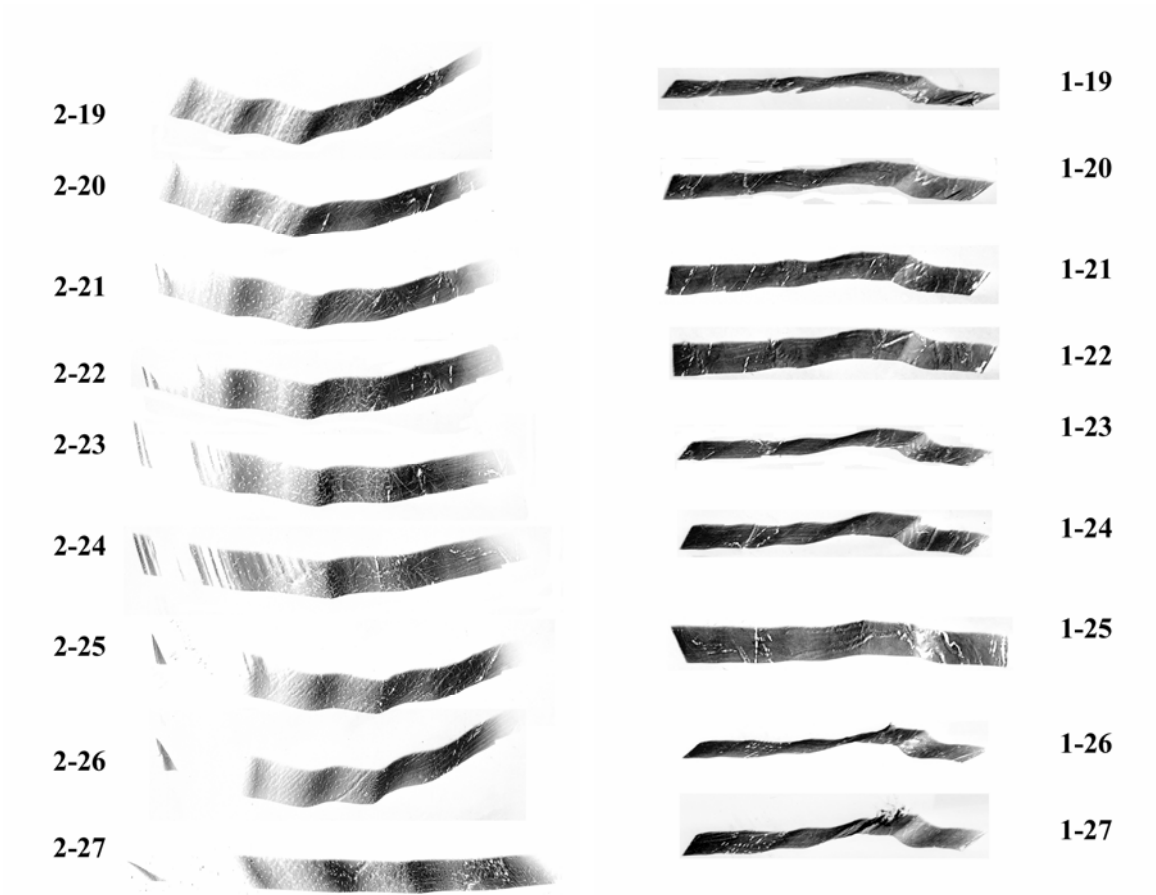


Figure 5. SWBXT images recorded from LGS-8 - Section C

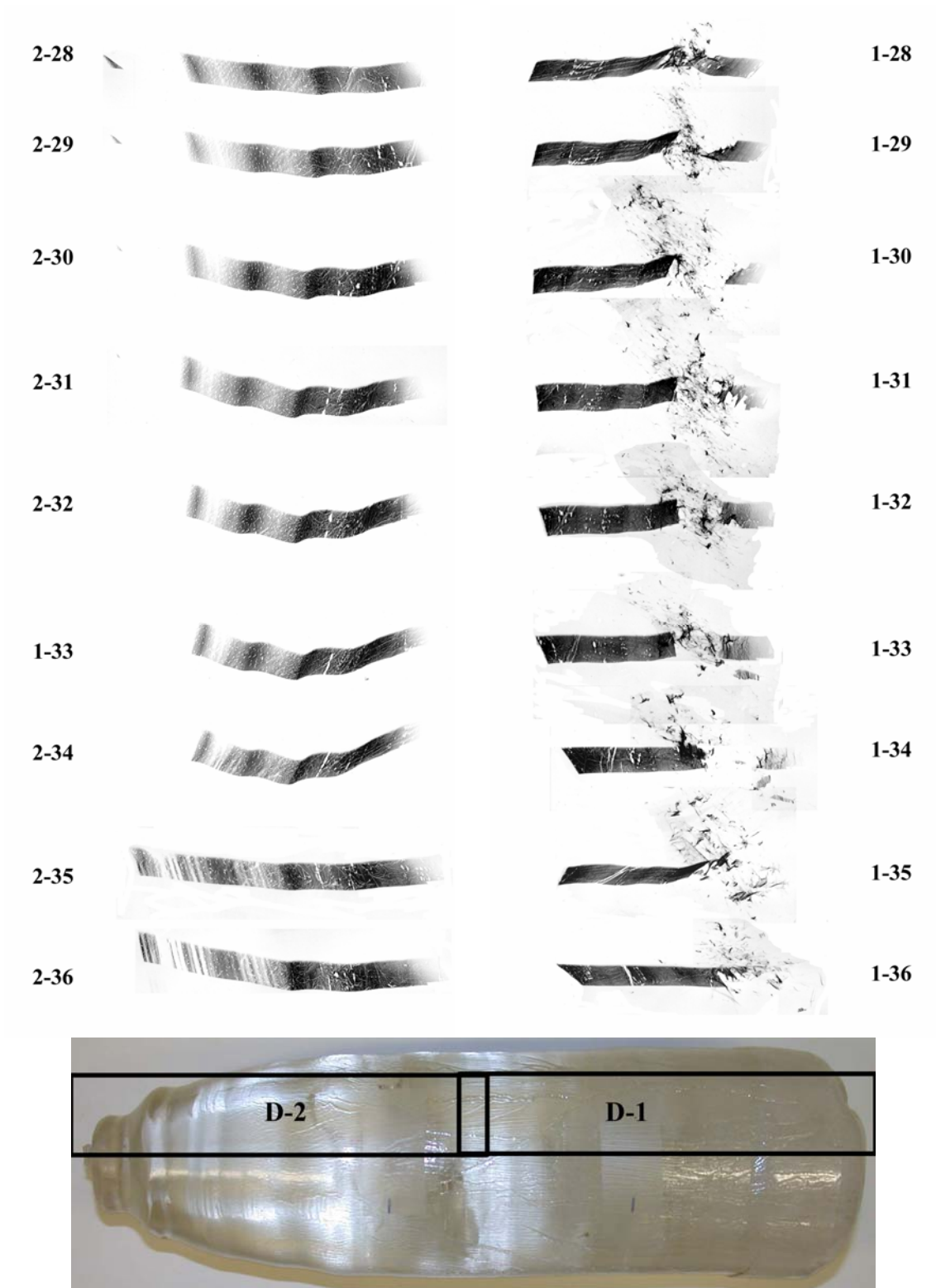


Figure 6. SWBXT images recorded from LGS-8 - Section D

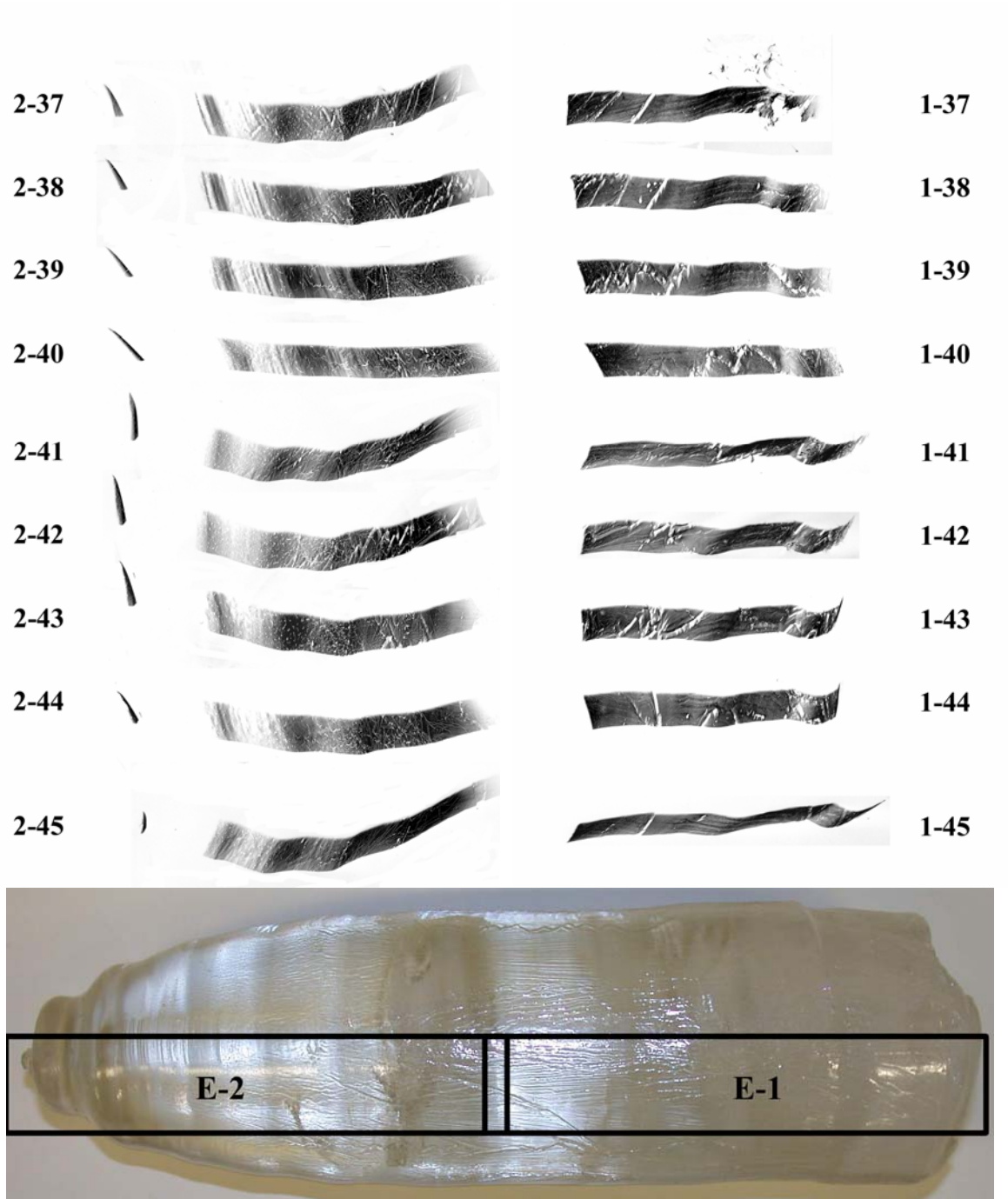


Figure 7. SWBXT images recorded from LGS-8 - Section E

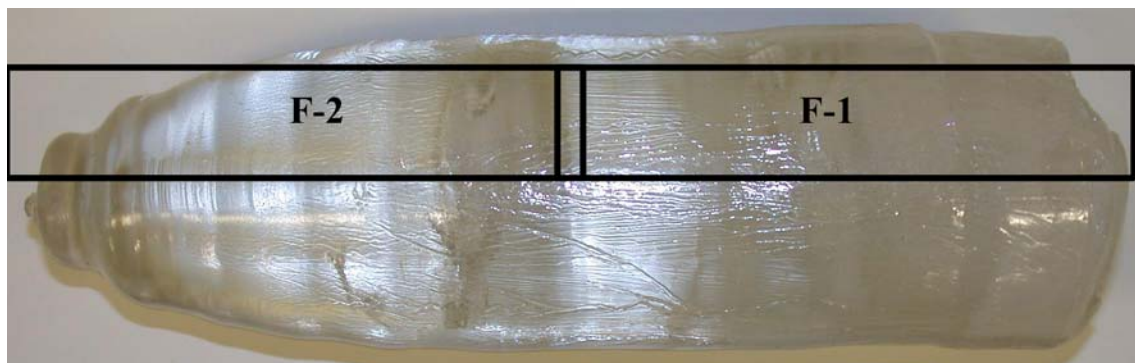
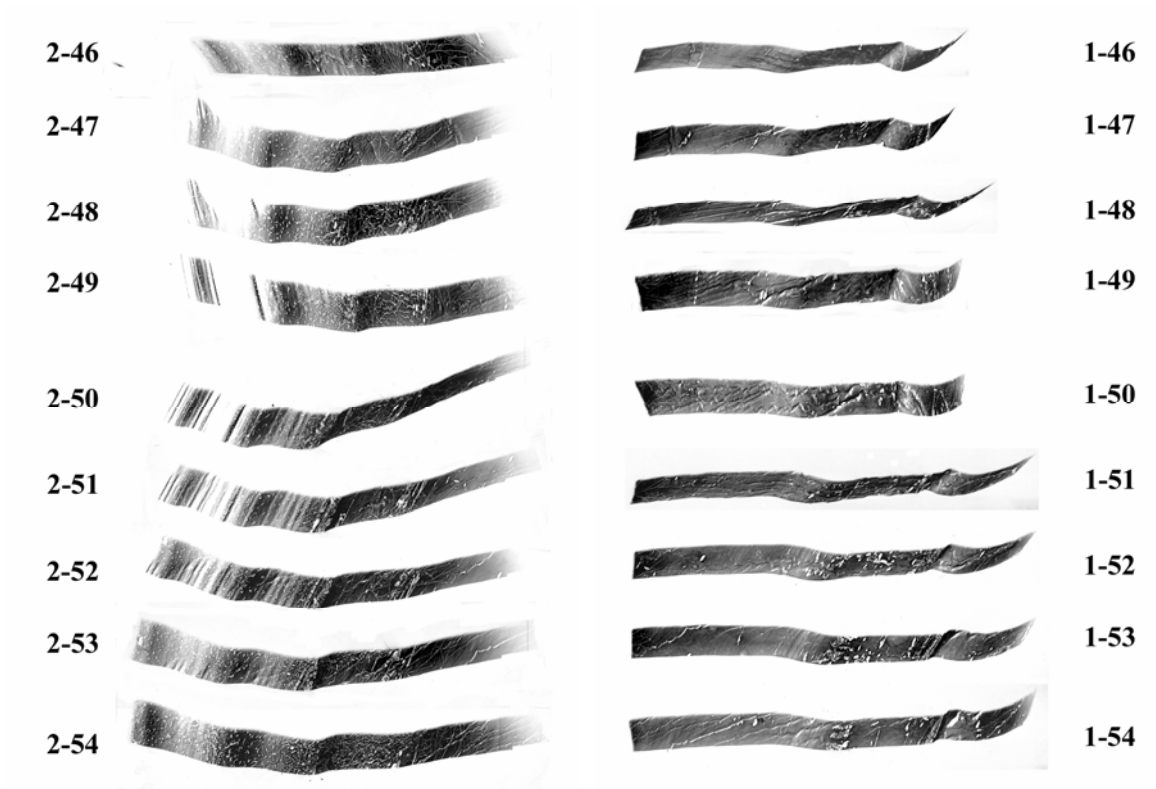


Figure 8. SWBXT images recorded from LGS-8 - Section F

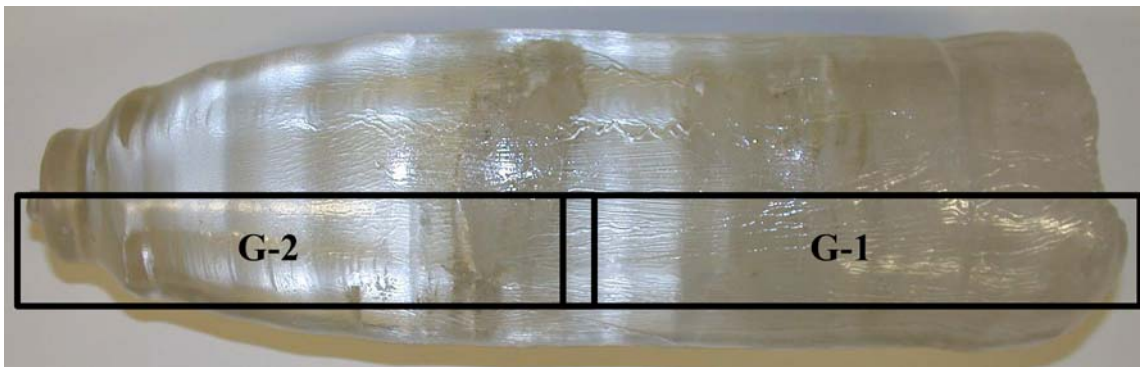
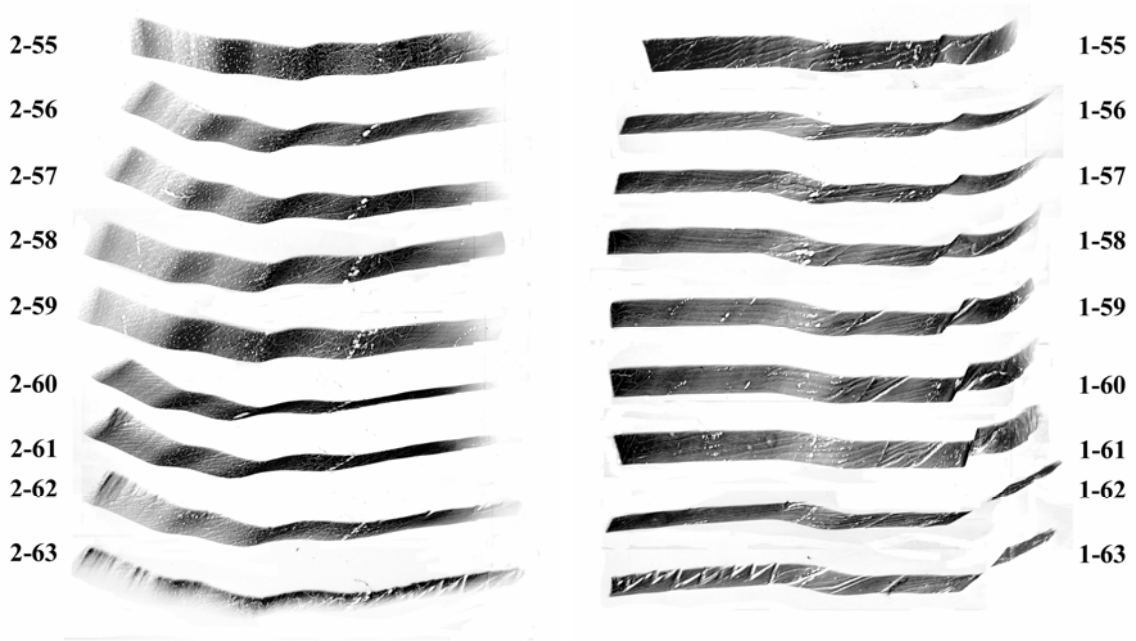


Figure 9. SWBXT images recorded from LGS-8 - Section G

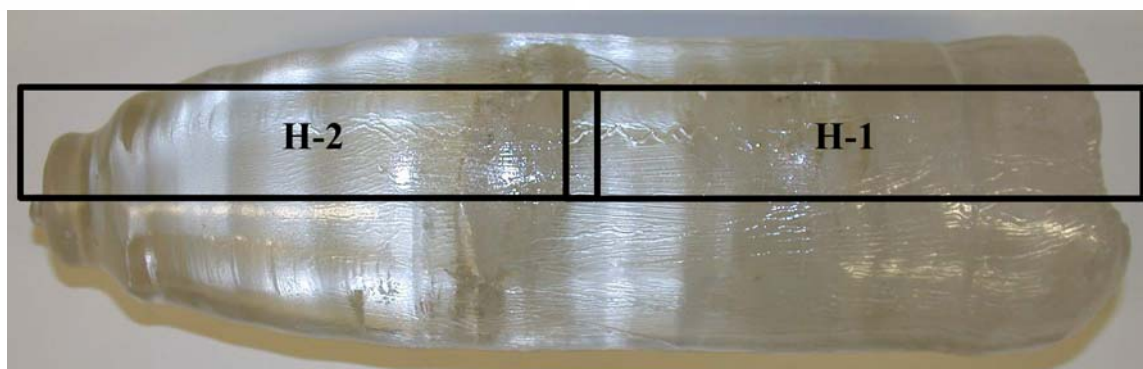
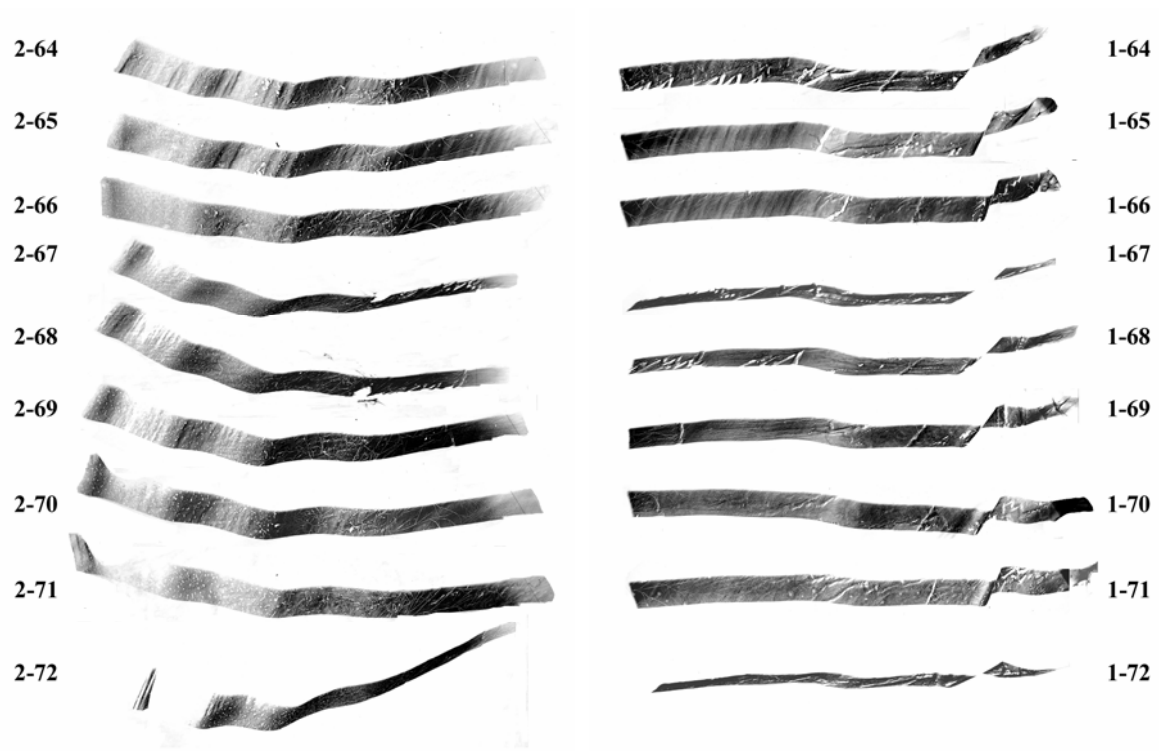


Figure 10. SWBXT images recorded from LGS-8 - Section H

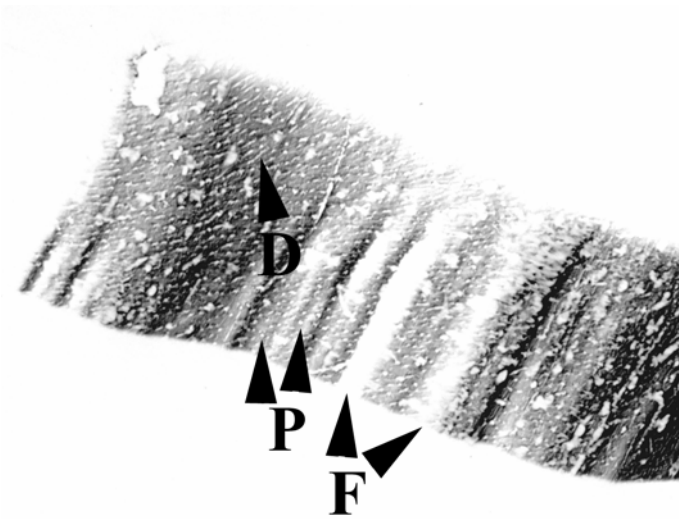


Figure 11. Enlarged 2-52 topograph showing precipitates, dislocations and facets

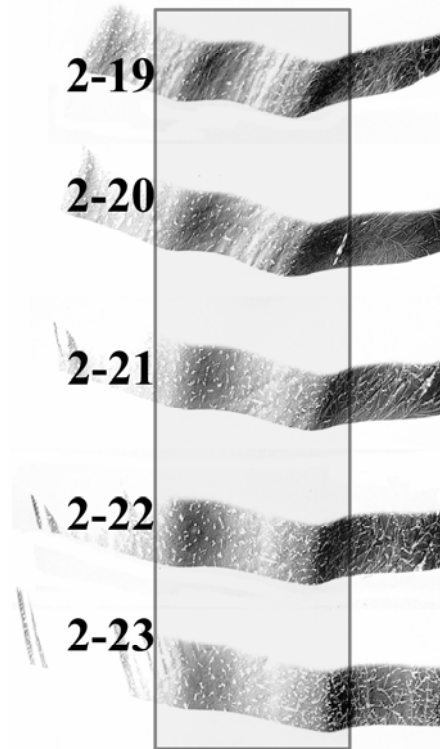


Figure 12. Inconsistent crystal growth near seed end

### STGS Boule

As the further development of research on LGS, LGN and LGT, two major disadvantages of those materials have been perceived. First, high  $\text{Ga}_2\text{O}_3$  content among

the raw materials makes the crystal cost much higher than quartz,  $\text{LiNbO}_3$  and  $\text{LiTaO}_3$ . Second, more importantly, the crystal structure of these compounds is “disordered”. The “disordering” results primarily from the fact that two of the cations in each compounds randomly share the same sites in the unit cell, for LGS,  $\text{Ga}^{3+}$  and  $\text{Si}^{4+}$  sharing the same two small tetrahedral sites; for LGT and LGN, the  $\text{Ga}^{3+}$  and  $\text{Ta}^{5+}$  or  $\text{Ga}^{3+}$  and  $\text{Nb}^{5+}$  sharing the same single octahedral sites. This causes randomly distributed distortion to the crystal structure, affecting the material uniformity and reproducibility and leading to lower than ideally achievable acoustic Q and electromechanical coupling.

Based on the “order-disorder” argument, several completely “ordered” langasite structure compounds have been developed, including  $\text{Sr}_3\text{TaGa}_3\text{Si}_2\text{O}_{14}$  or STGS,  $\text{Ca}_3\text{TaGa}_3\text{Si}_2\text{O}_{14}$  or CTGS,  $\text{Sr}_3\text{NbGa}_3\text{Si}_2\text{O}_{14}$  or SNGS and  $\text{Ca}_3\text{NbGa}_3\text{Si}_2\text{O}_{14}$  or CNGS. Here, some preliminary SWBXT results of STGS boule are presented.

An as-grown crystal of STGS was examined by SWBXT in the same way as the other four LGX boules. Fig. 22 shows the tail and seed end of the boule.

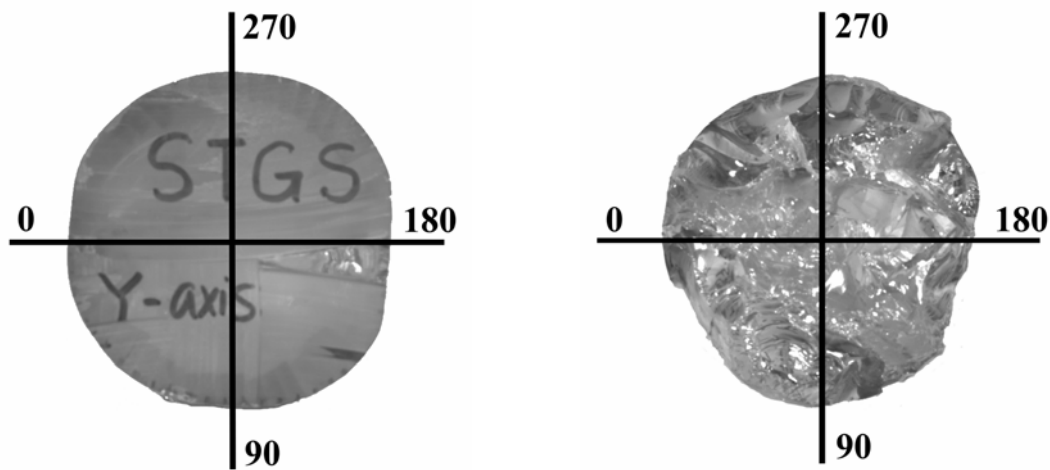


Figure 22. The tail and seed end of the STGS boule with the relative rotation angle positions.

Part of the topographs are presented, as before, in two groups with respect to the corresponding optical micrograph of the boule shown at the bottom of each group of topograph (see Fig. 23). There are no clear striation contrasts which can be observed in most of the topographs. Wavy contrast features, A, are caused by the ridges on the surface running along the length of the boule. Possible precipitate contrasts, P, can be observed throughout the whole boule. And other contrast due to surface roughness can also be observed.

This new STGS crystal tend to have very strong facet formation during crystal growth. Vertical white contrast features, F, observed in  $90^\circ \sim 180^\circ$  and  $180^\circ \sim 270^\circ$  quadrants, are produced by facet risers with the same formation mechanism as before in other LGX crystals. Some striation-like contrast can be observed in the facet area, but, in this case, it is not clear if it is from striations or due to surface features. Enlarged topograph (i) in  $90^\circ \sim 180^\circ$  quadrant, Fig. 24, clearly show this unique contrast feature

distinguishing it from LGN and LGT crystals.

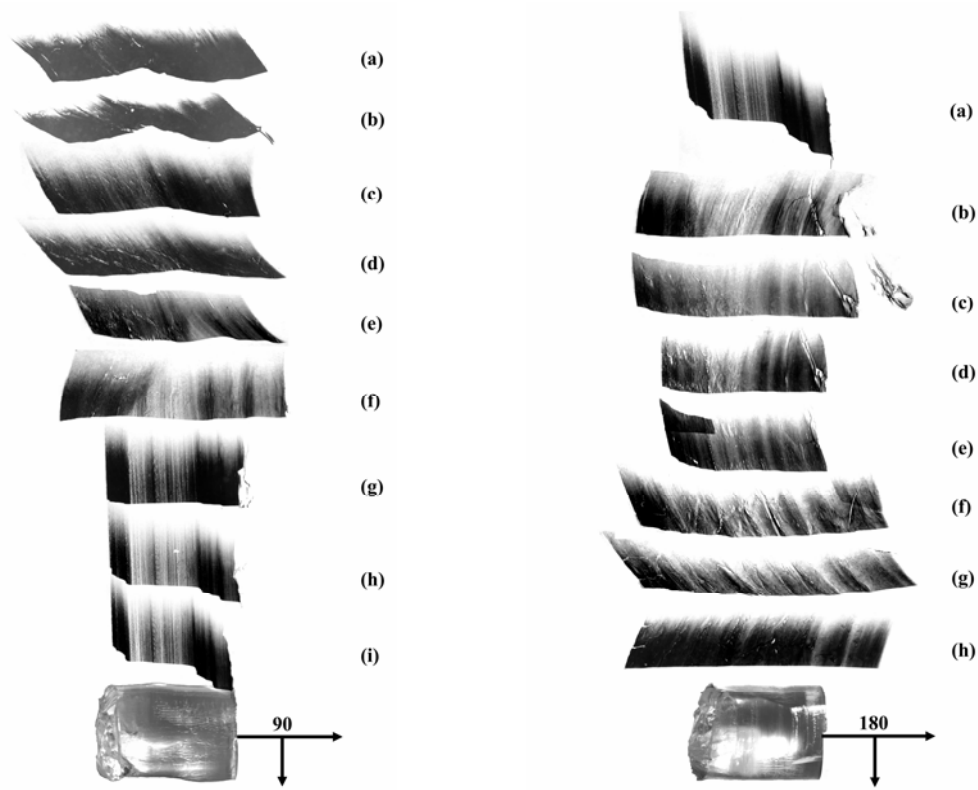


Figure 23. SWBXT images recorded from STGS boule

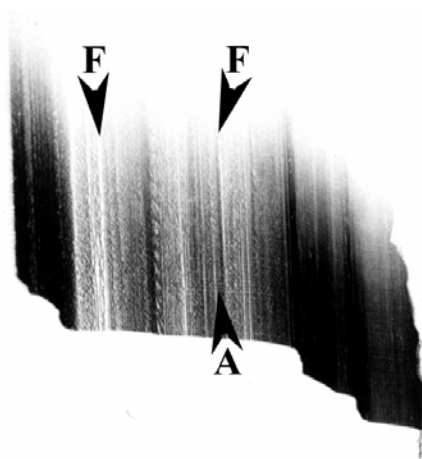


Figure 24. Enlargement of topograph (i) in  $90^{\circ} \sim 180^{\circ}$  quadrant showing wavy surface feature, A, and vertical white contrast facet features, F, along with some striation-like contrast

## Topography of LGX and Related Wafers

### Expected Geometry of Striations in LGX Wafers

Based upon the observations of striations in the LGX boules one can postulate their three-dimensional configuration inside the crystal. The striation shape follows that of the growth interface. A postulated configuration of growth interface shape and therefore striation shape for [001] growth axis in LGX single crystals is shown in Fig. 2-10. In wafers, the observed configurations will depend on the orientation of the wafer with respect to the boule. Possible striation configurations in Y-cut ([001] direction) and Z-cut ([100] direction) are predicted to be as shown in Figure 25. These predictions were confirmed in this work.

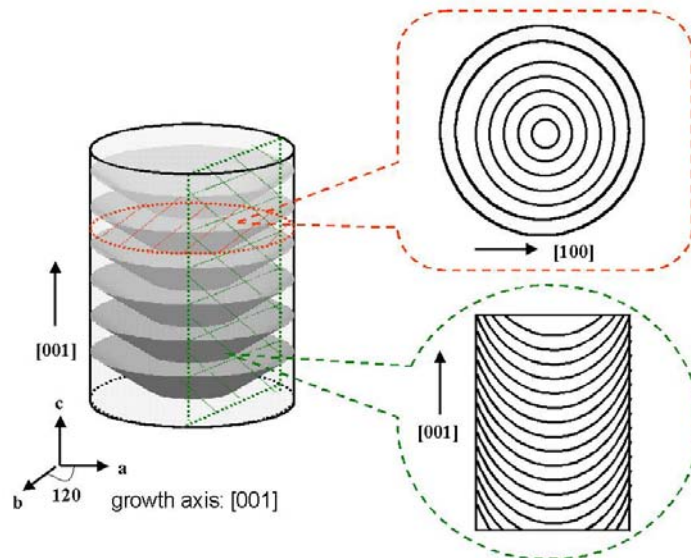


Figure 25. A possible configuration of interface shape/growth striations in LGX crystals

For example, LGX wafers cut from as-grown crystals were examined by SWBXT. Wafers are either Y-cut blanks (cut parallel to the growth axis) or Z-cut blanks (cut perpendicular to the growth axis).

For example Figure 26(a) shows a transmission topograph recorded from a Y-cut LGN wafer cut parallel to the [001] growth axis. Well defined contrast of a curved set of striations, K, can be observed in the topograph. Numerous band-like nearly white contrast segments, D, are likely to be dislocations running through the wafer from bottom to top; the one very long segment is likely to be a group of growth dislocations running at a small angle to the growth axis. Some surface artifacts and scratches, S, can be observed. Precipitates or inclusions, P, are evenly distributed throughout the whole sample. In addition a linear row of inclusions, I, can also be discerned.

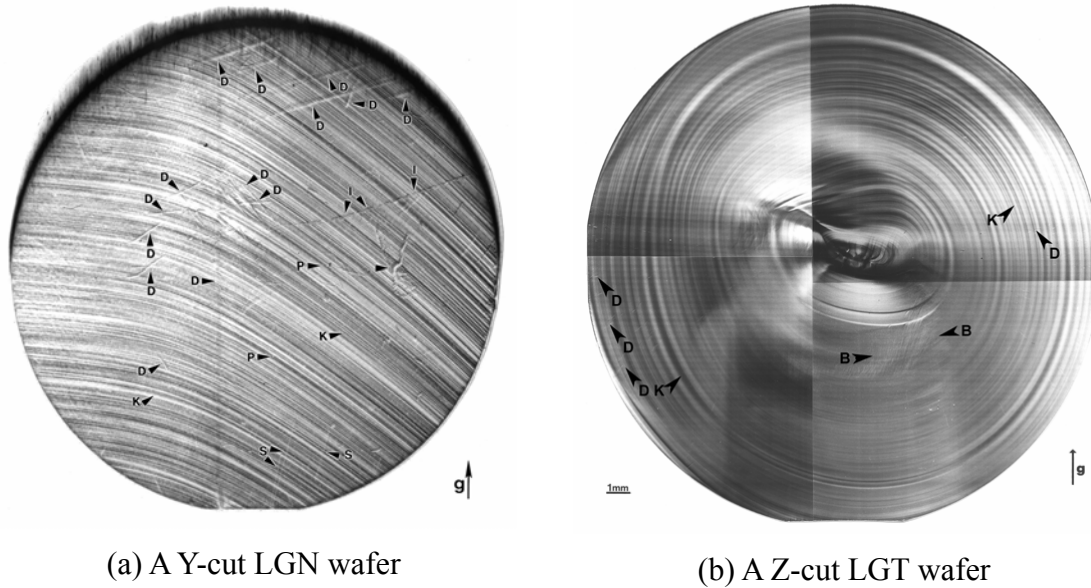


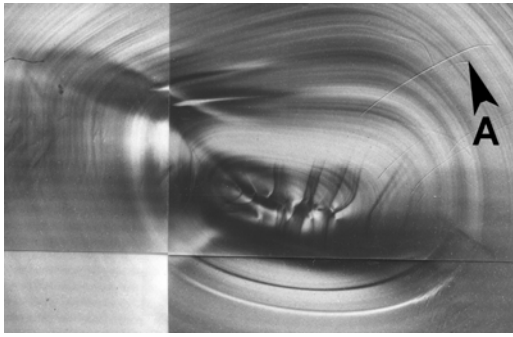
Figure 26. Transmission topographs recorded from two LGX wafers with  $g = 0002$

Figure 26(b) shows a transmission topograph recorded from a Z-cut LGT wafer cut perpendicular to the growth axis. A series of such topographs were recorded from eleven Z-cut wafers cutting from one LGT boule. These images comprised "snapshots" of the local interface shape in the wafer volume during the crystal growth process. Slight modifications were observed from wafer to wafer, reflecting the evolution of interface shape during the crystal growth.

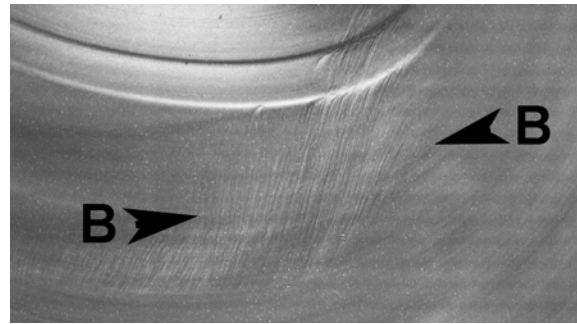
Fig. 26(b), clearly shows the well-defined contrast of the roughly concentric striation rings. The concentric striations indicate that the growth interface is either concave or convex, rather than flat; and indicate the presence of slight lattice parameter fluctuations during the crystal growth process. The periodicity of these striation configurations is indicative of the periodicity of the growth fluctuations that gave rise to them. The asymmetry observed in these roughly concentric striation rings reveals an asymmetry in the thermal field inside the growth chamber.

Note in the core region, Fig. 27(a), irregular striation rings in the center of the crystal indicate uneven growth near the core of the crystal; possible interface breakdown close to the crystal core is also observed, along with the attendant inhomogeneous distortion. Features similar to this were found in all such wafers, Fig. 27(a). The asymmetry of the interface shape in the central region is apparently propagated throughout the crystal.

Dislocation slip bands that appear to originate from the inhomogeneous distortion generated by the irregular interface shape are visible as several bands marked as B running across the middle section of the sample, Fig. 27(b). In all wafers, the central region is invariably surrounded by slip bands and generally is the region with highest dislocation density, further emphasizing the lower crystal quality in this region. These slip bands are possibly generated by the thermal stresses, which accompany the irregular interface shape and growth in this region.



(a) Detail of the core region



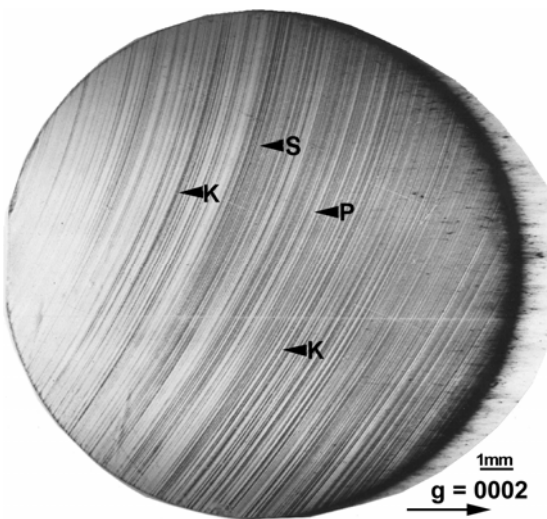
(b) The surrounding slip bands

Figure 27. Enlargement of the core region and the surrounding slip bands

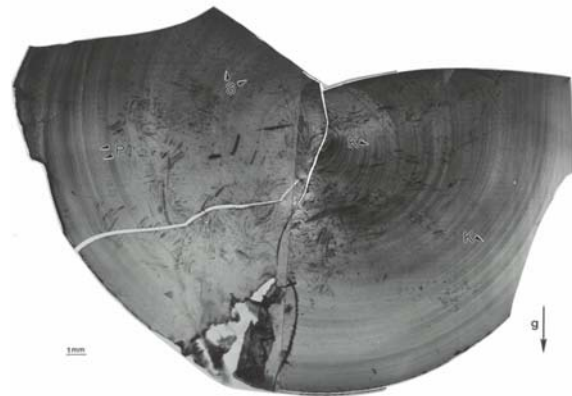
## LGN Wafers

### *LGN Wafers*

Typical SWBXT images recorded from Y- and Z-cut LGN wafers are shown in figure 28.



(a)



(b)

Figure 28 (a) transmission SWBXT image recorded from a Y-cut LGN wafer. Note the growth striations K, and precipitates, P; (b) transmission SWBXT image recorded from a Z-cut LGN wafer, showing striations K, and precipitates, P. S is a scratch.

Striation structures similar to those observed in LGS and LGT are revealed, along with a few dislocations and a distribution of precipitates. Further details can be seen in the enlargements presented in figure 29.

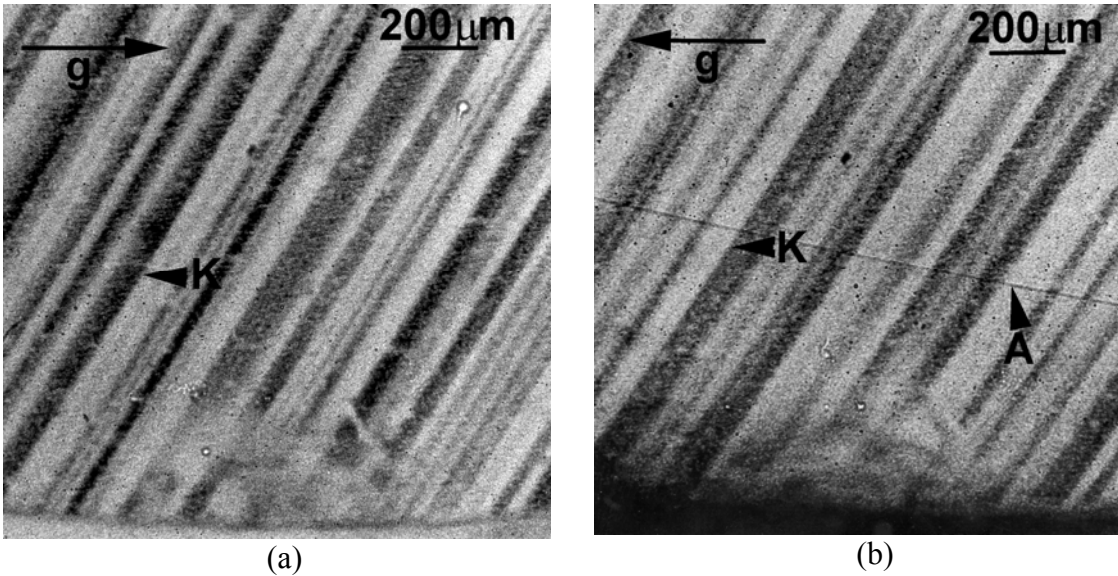


Figure 29. (a) and (b) Stereo pair of transmission images recorded from an LGN wafer, showing the reversal of contrast (e.g. at K) upon reversal of the active reciprocal lattice vector. Note the distribution of precipitates (white spots) throughout the image.

Figure 29 is actually a stereo pair (in this case a Friedel pair) of images which demonstrates that contrast reversal is obtained when the active reciprocal lattice vector is reversed. This helps shed considerable light on the mechanism of contrast formation for the striations, as demonstrated for the case of striations in S-doped LEC grown InP single crystals. The small white spots distributed throughout figure 29 (a) and (b) are precipitates. These can be seen more clearly in the enlargement shown in figure 30(a). In the enlargements shown in Figures 30(b) and (c), sinusoidal-like interface instabilities can be observed at C. This is likely to be due to the onset of constitutional supercooling. Similar effects have been observed by our group in Czochralski grown InGaAs single crystals.

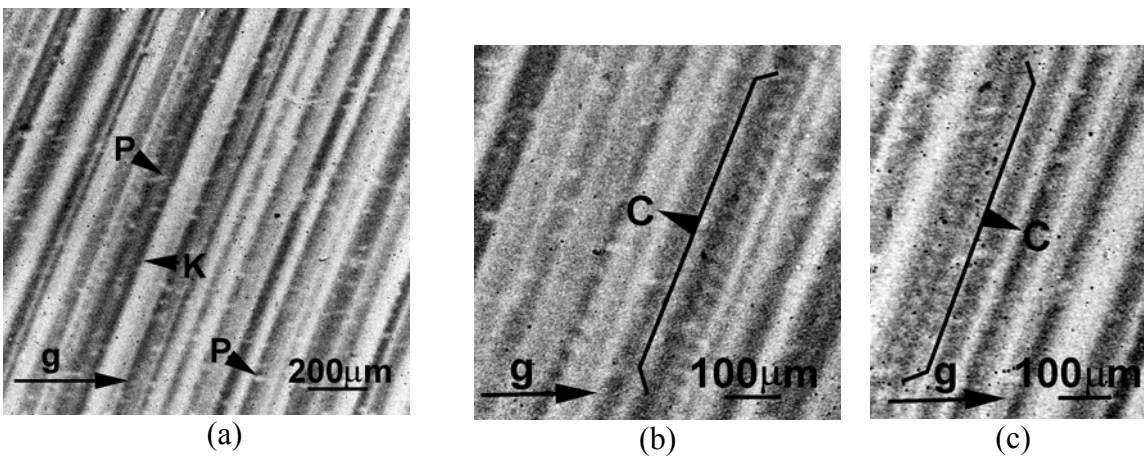


Figure 30. (a) Enlargement from image similar to 28(a) showing the distribution of precipitates, P; (b) and (c) enlargements showing the onset of sinusoidal-like instabilities in the interface shape, indicative of the onset of constitutional supercooling.

## LGT Wafers

### *Facet formation in LGT Crystals*

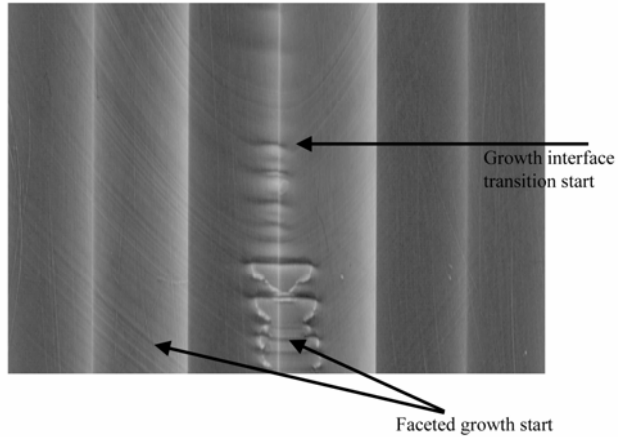


Figure 31. Optical micrograph showing central core region and facets

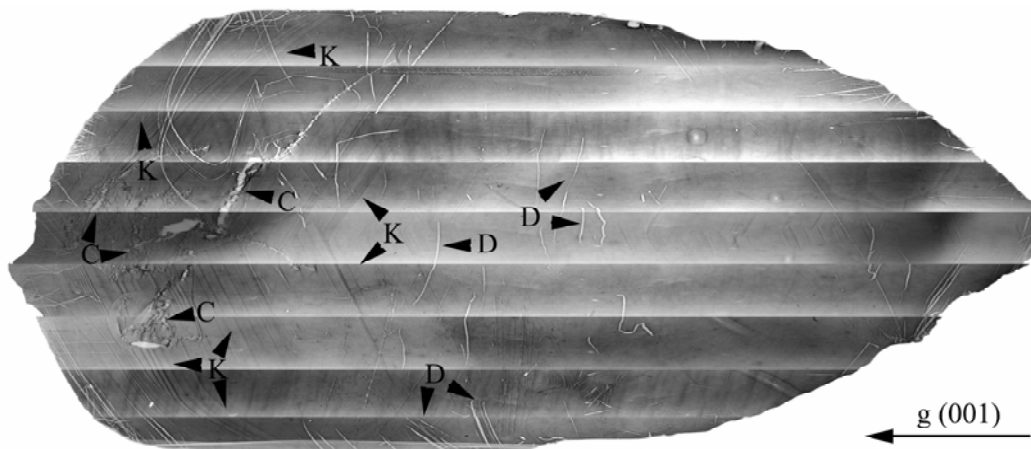


Figure 32. Topograph recorded from Z-cut plate of LGT. Note the straight striation images, K, indicative of faceting. C indicates cracks, D dislocations

On topographs recorded from Z-cut plates, straight striation bands indicate the presence of flat growth facets (see Figure 32). Faceted growth requires a larger supercooling than growth with a rough surface and the interface advances periodically rather than continuously. With an overall convex interface shape, and diffusion-control growth, facets can form when the isotherm becomes normal to a favored plane.

At the junction between the facets near the core of the crystal, high stresses and strains are expected, giving rise to high dislocation density, cracking or incorporation of inclusions. Facet control is usually achieved by interface shape control, which is controlled by two types of melt convection, natural and forced convection, by proper seeding, fast rotation etc. With a flat interface and facet formation, striations will mainly lie in a plane and be perpendicular to the growth direction.

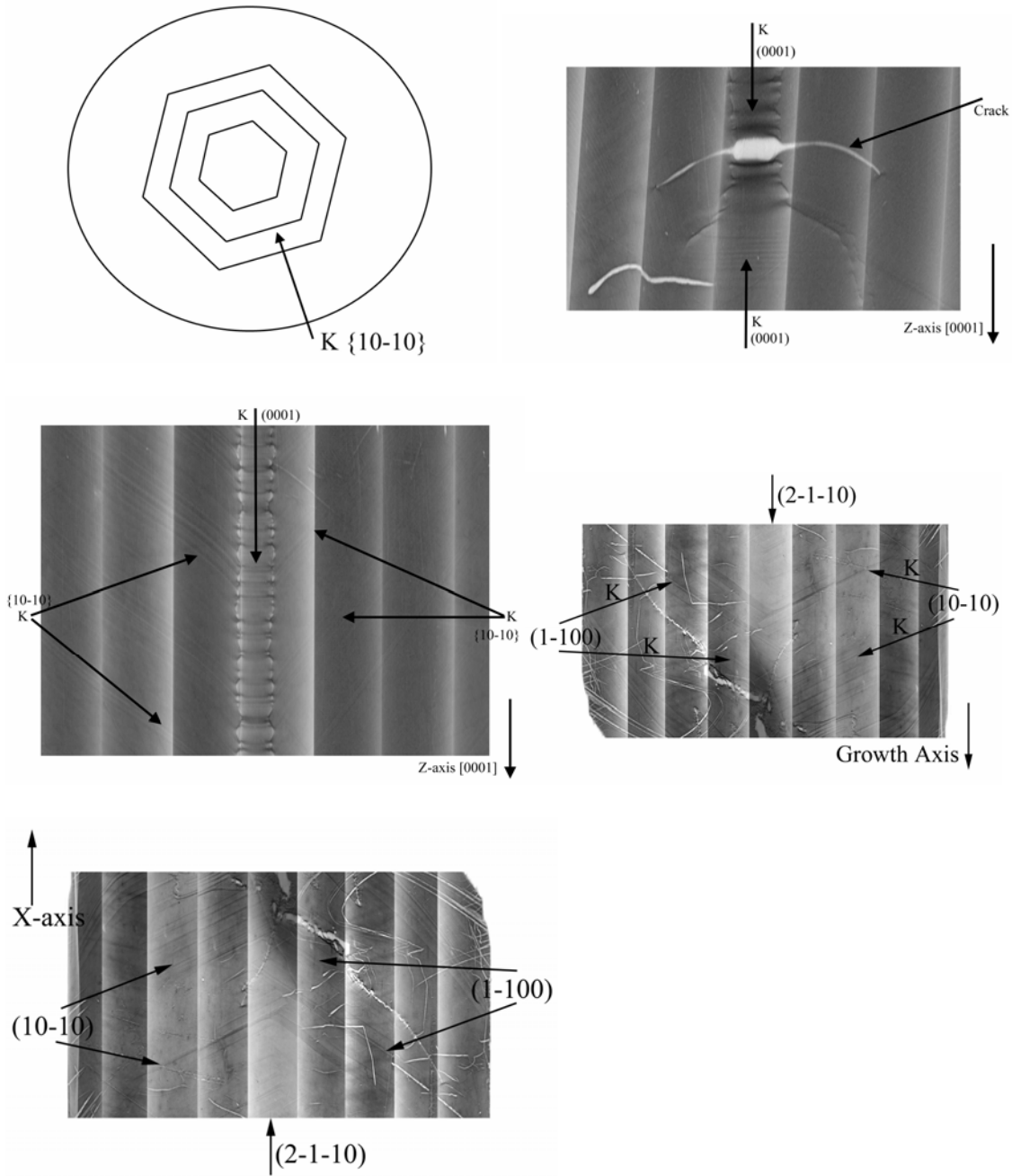


Figure 33. Discontinuous growth on the (10-10) and (1-100) facet planes leads to facet

formation.

### CTGS Wafers

Two CTGS crystals (Grown by C. Klemenz at the U. of Central Florida) of 10-10 surface orientation (Y-cut) were studied using SWBXT in the transmission geometry. The heavy elements (Ta and Ga) that are present in CTGS lead to quite high X-ray absorption coefficients. The samples studied were around 500 microns in thickness so that dynamical contrast effects are most likely to be observed on the topographs.

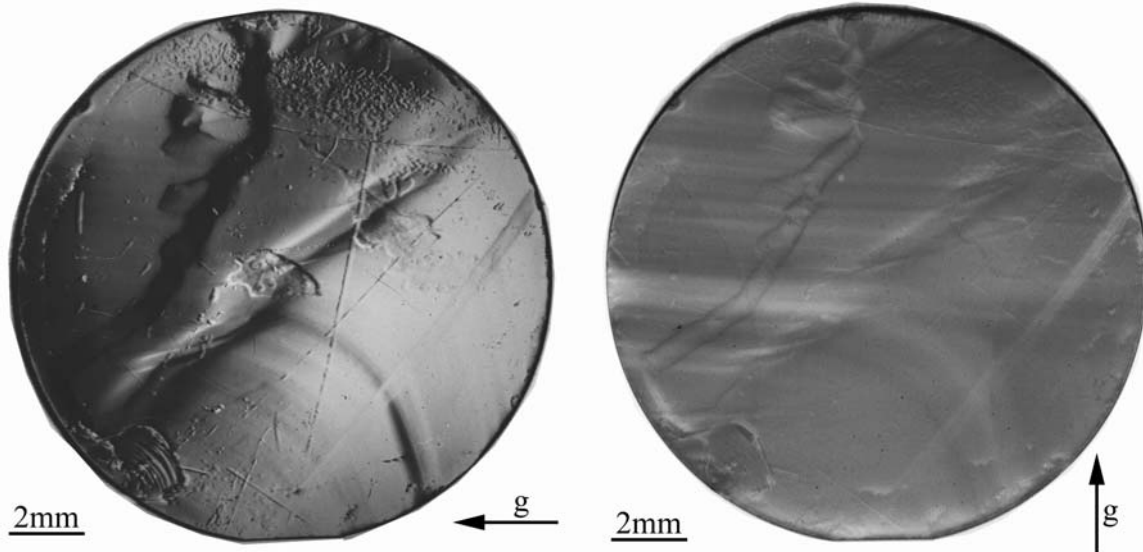


Figure 34. SWBXT images recorded from first CTGS crystal wafer. (a)  $g=0001$ , wavelength, 0.88 Angstroms; (b)  $g=1-210$ , wavelength, 0.70 Angstroms.

Figure 34 shows two images recorded from one of the two crystals. The dominant contrast features are the growth striations and the features delineating the core region of crystal. Either side of this core region, the striation pattern changes from a highly curved configuration to a faceted configuration. A distribution of inclusions is also observed throughout the wafer. There are also a few scratches and other surface artifacts evident on the image.

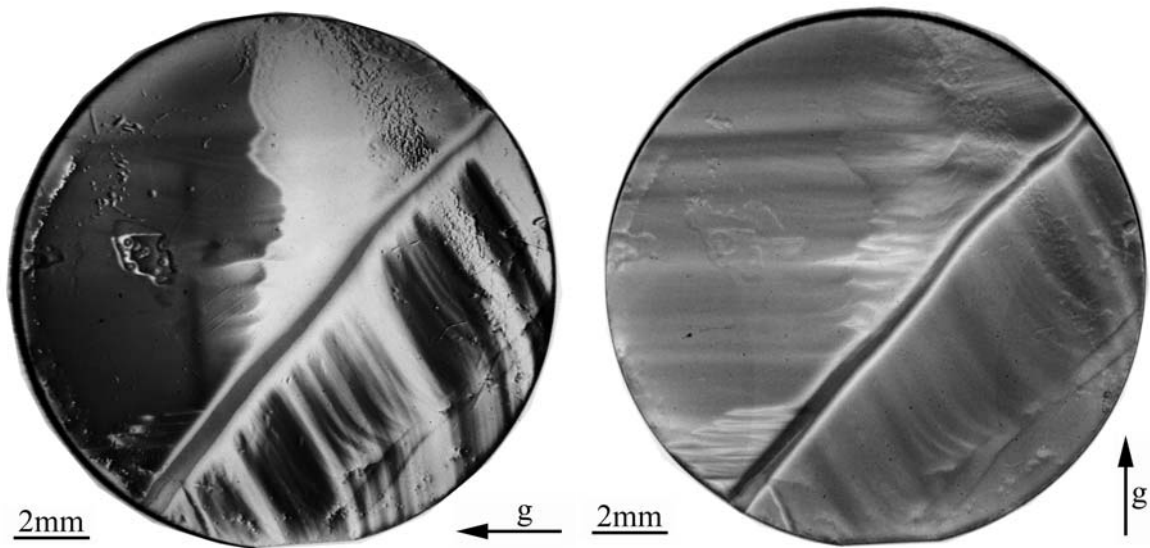


Figure 34. SWBXT images recorded from second CTGS crystal wafer. (a)  $g=0001$ , wavelength, 0.88 Angstroms; (b)  $g=1-210$ , wavelength, 0.70 Angstroms.

Figure 34 two shows topographs recorded from the second CTGS wafer. The dominant feature again is the growth sector boundary which separates two sections of crystal which have different striation patterns. Note that contrast from striations on the upper left section is almost invisible in the 0001 reflection since the diffraction vector ( $g$ ) is parallel to the striations (i.e. displacement vector associated with striations is perpendicular to its line (plane in 3D)). Again, it is possible that this boundary divides the faceted and non-faceted sections of the boule. The band running below to the right also appears to be a growth sector boundary. Closer observation of this band reveals fringe contrast usually associated with such boundaries. In the upper section, contrast observed appears to be from surface features – under the optical microscope these appear as small cracks. Inclusions are also observed distributed throughout the wafer.

Results from the studies of these two CTGS samples show:

- 1) Growth striations are the most dominant defects in the CTGS crystals. Growth striations are short-range periodic compositional variations leading to corresponding lattice parameters fluctuations due to crystal growth rate variations. Growth rate variations are due to temperature gradients driven by hydrodynamic flows to the growth interface. Striations are not visible optically; and no report exists of striations being revealed by chemical etching or other techniques; the presence of striations could only be revealed by X-ray topography;
- 2) The spacing of growth striation bands reveals the periodicity of the striations, which is the direct indication of the periodicity of the growth rate variations during the crystal growth;
- 3) The symmetry of the striations, both the concentric striation rings and striations revealed in length-wise cut slices, indicates the control of the

symmetry of the thermal field inside the growth chamber;

- 4) Faceting can also introduce striation bands, called “macro-step striations”, into the crystal, shown in Figures 1 and 2. Straight striation bands indicate the presence of flat growth - facets, i.e. discontinuous growth on the (10-10) and (1-100) facet planes. Faceted growth requires a larger supercooling than growth with a rough surface and the interface advances periodically rather than continuously. With an overall convex interface shape, and if diffusion control operates, facets can form when the isotherm becomes normal to a favored plane such as (10-10) and (1-100).
- 5) The “core region” in the crystal should be removed or greatly reduced in order to improve the overall quality. Such a “core region” has the highest thermal stress and possibly highest dislocation density with great inhomogeneous distortion. It is the main cause of cracking in these crystals.
- 6) Dislocations and precipitates are both common defects presented in CTGS crystals.

## Topography of LGX Resonators

Topographs recorded with resonators fabricated from two different LGN crystal boules, LGN-4 and LGN-8 are shown in Fig. 35(a) and (b) respectively.

Well-defined sets of striations K can be observed in all resonators from both boules. However, the striation contrast visible on wafers cut from boule LGN-4 was much sharper and more well-defined than that visible on wafers cut from LGN-8. Strain contrast associated with the edge of the electrode superimposed on the striation contrast. Surface dominant contrast associated with the interaction between LGN sample surface and the electrode can be observed in all images. In the set of resonators cut from LGN-8, there are regions where the interface shape becomes grossly distorted. In those regions, the clarity of the striation images is further reduced. This indicates the differences in growth conditions or control for LGN-8 compared to LGN-4, and that the general quality of LGN-8 wafers is inferior to those from LGN-4. The interface distortion visible in LGN-8 wafers provides some evidence in favor of poorer inherent crystal quality. Further insight into the relative importance of these two possible contributory factors could be determined by further studies carried out with High Resolution X-ray Diffractometry and further SWBXT studies carried out after repolishing the crystals. Clear images of dislocations and inclusions are also observed on LGN-4 wafers but not on LGN-8 wafers. The poorer contrast obtained from LGN-8 wafers may arise from: poor inherent crystal quality (compared to LGN-4) and/or poor surface finish.

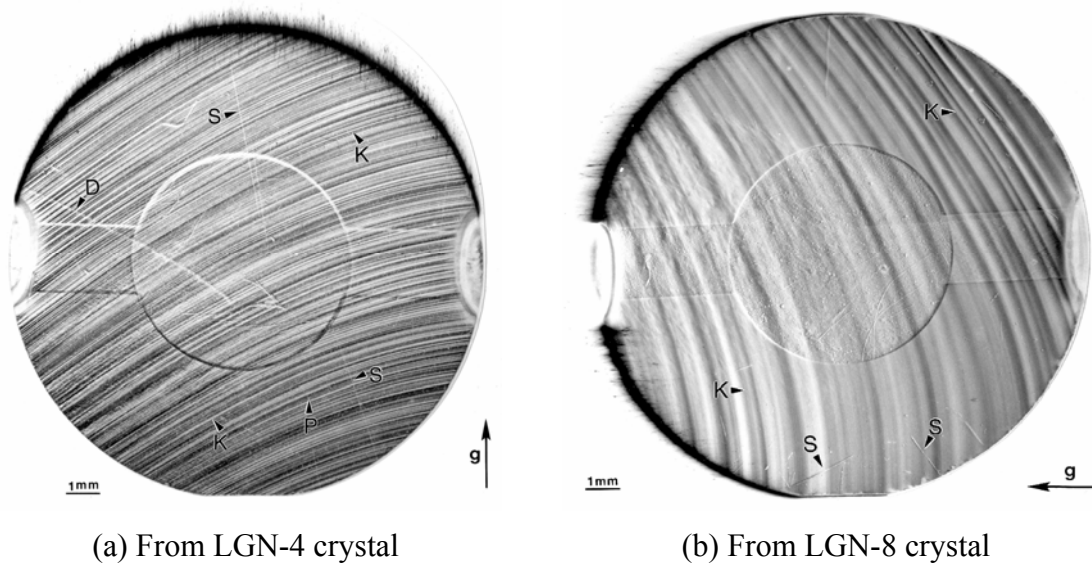


Figure 35. Transmission topographs recorded from LGN resonators

The attempt to correlate the LGN resonator microstructures with  $Q \cdot f$  factors has been carried out. However, all the resonators examined (from two different boules) had striations present, so the effect of striations on  $Q \cdot f$  could not be assessed directly. However, the surface quality of wafers from one boule was better than the other, might suggest a possible correlation.

### Discussion: Origins of Striations in LGX and Related Crystals and Strategies for their Avoidance

1. Striations are the most significant defects in LGX crystal growth.
2. In LGX, the striations are not visible optically. And there is no report of striations revealing in LGX by chemical etching or other techniques. The presence of striations was only revealed by X-ray topography, so far.
3. In LGX, the striations originate due compositional variations or non-stoichiometry in the melt. These can arise due to:
  - a. the small size or even absence of the field of congruent melting (where the melt composition is the same as the solid), due to the complexity of the ternary component system ( e.g.  $\text{La}_2\text{O}_3 - \text{Ga}_2\text{O}_3 - \text{SiO}_2$ );
  - b. small but finite evaporation of  $\text{Ga}_2\text{O}_3$  from the melt
4. This non-stoichiometry in the melt can also give rise to the effect of constitutional supercooling, which can drive interface breakdown or cellular growth. SWBXT images of LGN wafers cut perpendicular to the growth axis give out strong evidence.
5. To prevent striations, some possible ways are:

- a. carefully prepare starting melt composition;
- b. improve temperature control, keep growing proceed at a most exactly stoichiometric melt composition;
- c. reduce temperature fluctuation during crystal growth
- d. reduce evaporation by improving the growth atmosphere.

### **Discussion: Assessing the Influence of Striations**

1. Generally, in order for defects to significantly affect the Q factor, they must have some internal movement that does not respond instantaneously to an applied stress. They must be anelastic; as, for example, point defects with thermally activated relaxations between orientations and dislocations that bow out non-instantaneously in response to stress.
2. Since striations are associated with slight variations in crystal structure (variations in composition and lattice spacing), they will result in spatial variations of the elastic constants. However, they will not necessarily have an anelastic response to acoustic waves and, therefore, may not affect the Q factor. This depends on whether applied stress induces a slight restructuring of the atoms in the striations. So, a lack of effect on Q factor is possible.
3. On the other hand, it would be surprising if striations had no effect on the temperature independence of oscillators. Local variations of elastic constants are bound to produce changes in the bulk elastic constants (at wavelengths long compared to the periodicity of the striations) and their temperature derivatives. In addition, the effects can be expected to be different for different elastic constants, since striations have a directionality.

## **Quartz**

### **Study of Quartz Crystal Bar**

One synthetic quartz single crystal bar, grown by the hydrothermal method, was examined by SWBXT. The major surfaces of the lumbered quartz bar,  $\pm X$  and  $\pm Z$  surfaces are ground flat and mutually perpendicular, but the ends of the bar show the “natural” crystal faces. The orientation of X and Z surfaces is  $(2\bar{1}\bar{1}0)$  and  $(0001)$  respectively. The dimension of the quartz bar is roughly  $180\text{mm} \times 62\text{mm} \times 40\text{mm}$ .

X-ray topography in reflection geometry was used to study the defects features in the near surface regions of the crystal bar. Topographs were recorded covering the whole surface of all four major surfaces by moving the crystal bar in the direction perpendicular to that of the X-ray beam. Each topograph covers about 5mm width of the surface. Due to the geometry, the topographs suffer severe distortion along the horizontal direction, while along the perpendicular direction suffering almost no distortion.

Figures 36 and 37 show the reflection topographs of  $\pm X$  surfaces along with the photos of the surfaces.

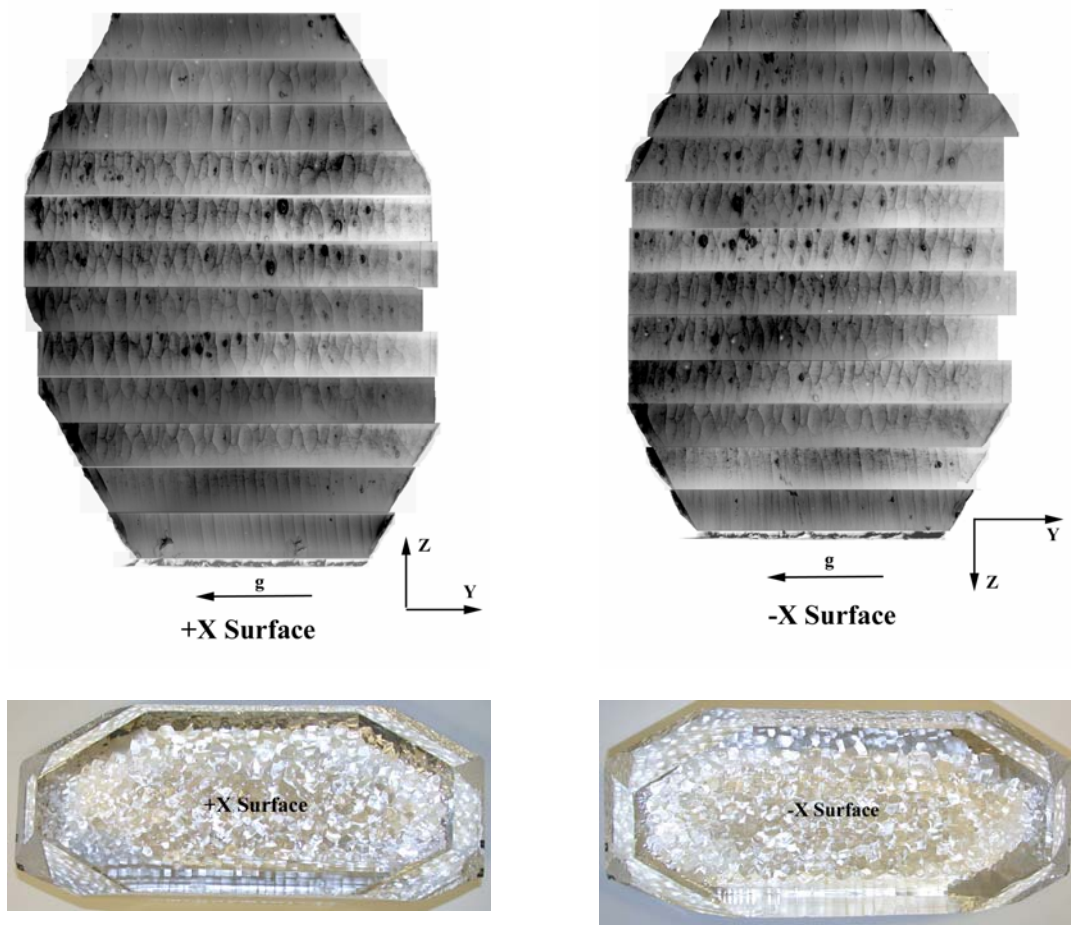


Figure 36. Topographs of quartz bar +X surface

Figure 37. Topographs of quartz bar -X surface

Most features shown on those topographs are the ripple features of the surfaces. Black irregularly shaped features were scattered throughout both surfaces with much higher concentration and bigger size in the middle of the crystal. Those are rows of emergent ends of cluttering dislocations, which may be decorated with impurities, constituting subgrain structures in the crystal. Most importantly, further examination reveals that some of the clutters of dislocations appear to be running through the whole crystal along the X direction ending at both sides of the X surfaces, which results pairs of subgrains showing on both sets of topographs. Figure 38 compares the subgrains shown in the 5th and 6th strips of both sets of topographs, in which three pairs of subgrains, among others, are shown linked together side by side. At least half of the subgrains on one set of the topographs can find their twin on the other set of the topographs.

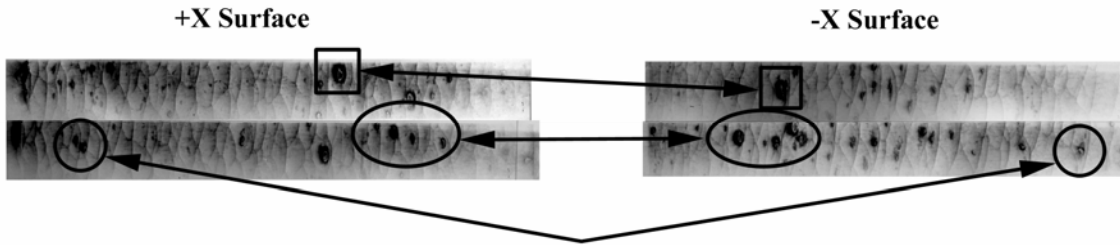


Figure 138. Paired subgrains on +/-X surfaces

Figure 39 and 40 show the reflection topographs of  $\pm Z$  surfaces along with the photos of the surfaces.

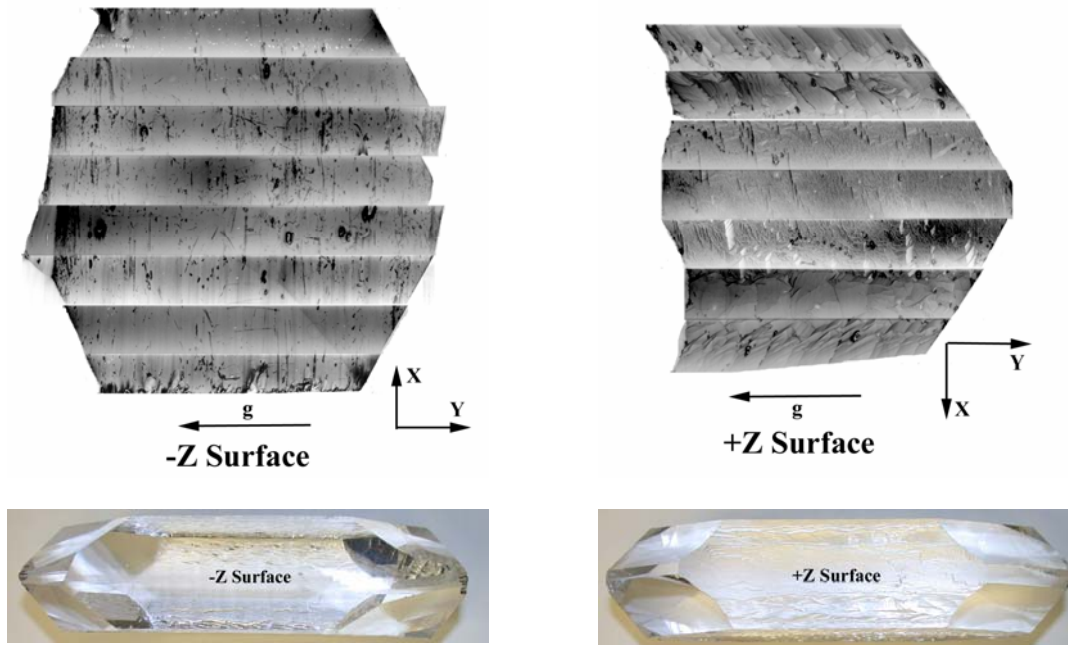


Figure 39. Topographs of quartz bar -Z surface      Figure 40. Topographs of quartz bar +Z surface

Other than the dominant surfaces features (namely artifacts and scratches), dislocations are clearly visible on both sets of topographs, especially on  $-Z$  surface. Groups of dislocations, indicated by D in Figure 41, run through the crystal along the X direction starting/ending at the X surfaces. This observation apparently is correlated to the twin subgrains on  $\pm X$  surface. Although the one on one correlation between the dislocations and the twin subgrains can not be established at this time, it certainly confirms that the twin subgrains on  $\pm X$  surfaces are rows of dislocations running through the whole crystal along the X direction.

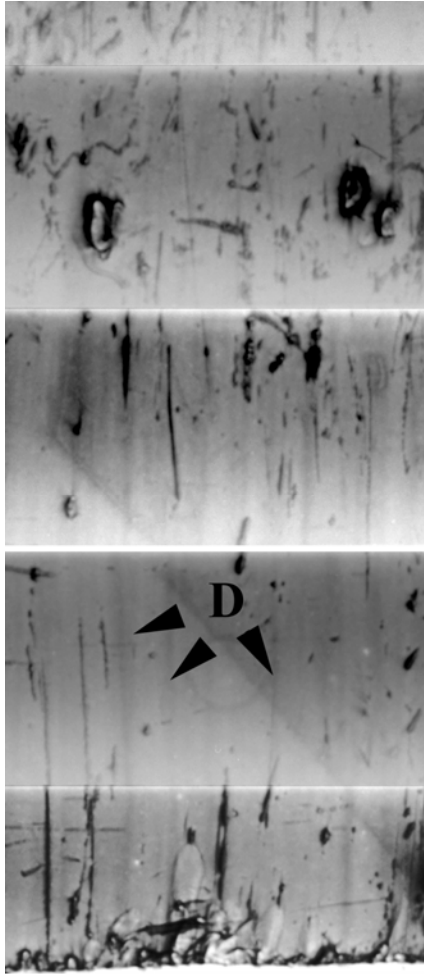


Figure 41. Dislocations on -Z surface parallel to X direction

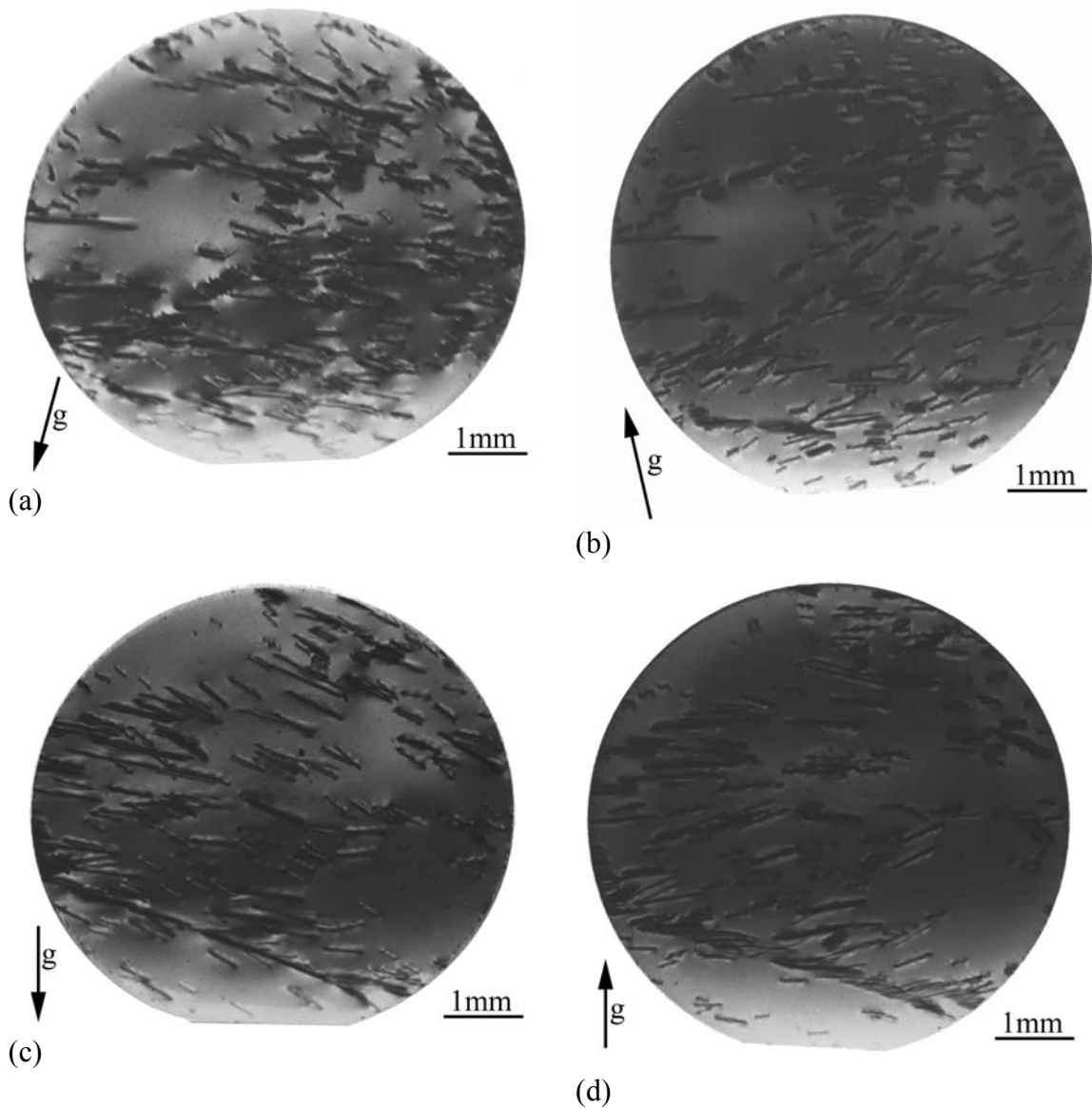
Inclusions or precipitates are visible in the +Z surface topographs. Subgrains with smaller size are also distributed on the -Z surface whose origins are not clearly known for now.

The dislocations/twin subgrains can greatly influence the mode shape of the quartz crystal; hence it would be a major factor determining the performance of the quartz crystal devices. Further study should be conducted to determine the origin of the dislocations/twin subgrains and how they will affect the performance of the devices. Because no two quartz bars will have exactly the same distribution of defects, they should be routinely screened before manufacture of high precision quartz crystal devices.

### **Study of Quartz Crystal Wafers**

SWBXT imaging was carried out on one batch of four quartz wafers and on a second batch of three quartz wafers. Complete defect analysis was carried out on all wafers.

For the first batch of four wafers, the surface orientation was close to (23-54). Figure 42 shows images recorded from all four wafers. Two reflections are presented for the first two wafers and three for the last two. Each crystal shows straight dislocation segments inclined to the surface of the wafer and a few inclusions. Occasionally the dislocations appear to organize into boundaries. In view of the low dislocation density and relatively high product of absorption coefficient and thickness, dynamical diffraction conditions operate and dislocation images comprise three parts: a kinematical image (dark line), a dynamical image (white contrast adjacent to the dark line), and an intermediary image (fringe contrast due to the inclination of the dislocation to the surface).



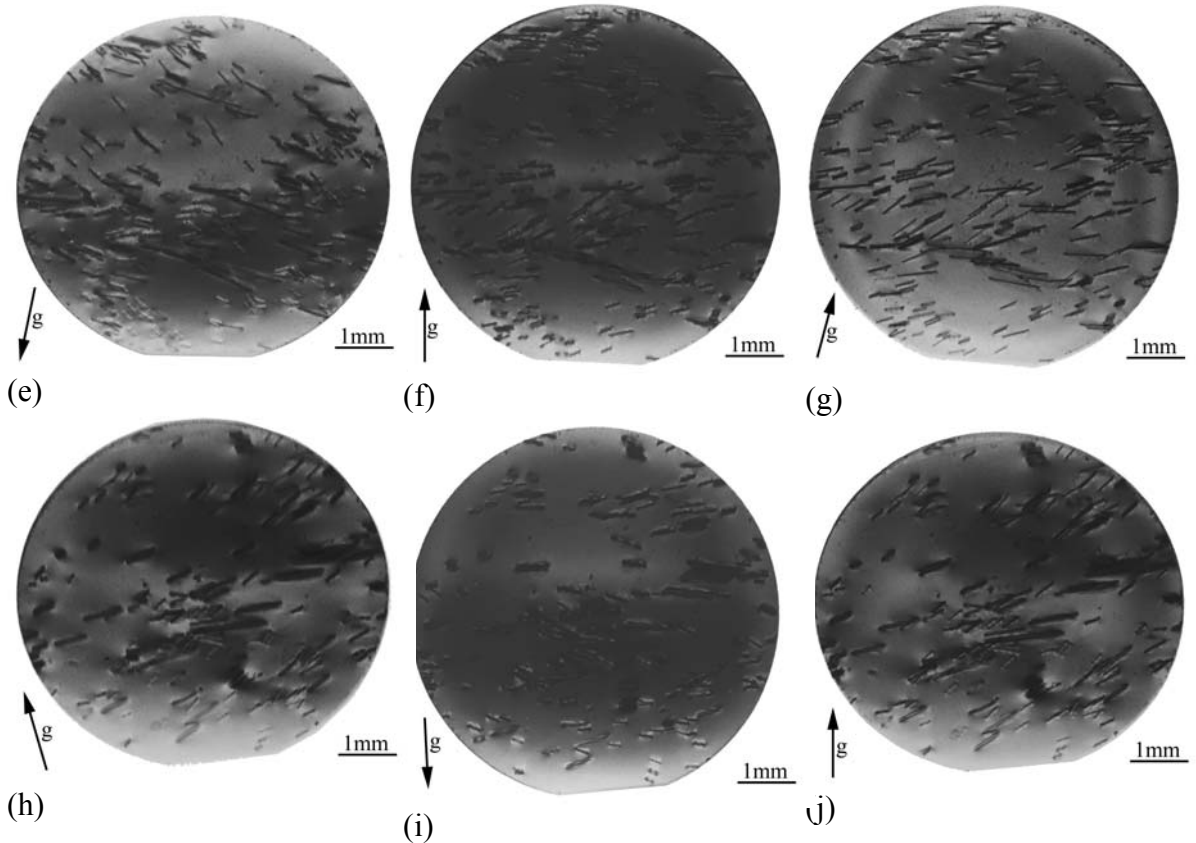


Figure 42. SWBXT images recorded from four different quartz wafers: Wafer 1: images (a)  $g=-12-10$ , wavelength 1.11 Angstroms and (b)  $g=2-200$ , wavelength 0.83 Angstroms; Wafer 2: images (c)  $g=-12-10$ , wavelength 1.11 Angstroms and (d)  $g=2-200$ , wavelength 0.69 Angstroms; Wafer 3: images (e)  $g=-12-10$ , wavelength 1.34 Angstroms, (f)  $g=2-200$ , wavelength 0.69 Angstroms, and (g)  $g=3-301$  wavelength 0.80 Angstroms; Wafer 4: (h)  $g=-12-10$ , wavelength 1.34 Angstroms, (i)  $g=2-200$ , wavelength 0.69 Angstroms, and (j)  $g=2-31-1$  wavelength 0.80 Angstroms.

Figure 43 shows images recorded from the second batch of three quartz crystals. The overall dislocation density in this batch of wafers is lower than in the first batch suggesting improved device performance. This is a subject of future investigation. The dislocations are also inclined at a larger angle to the surface than in the first batch.

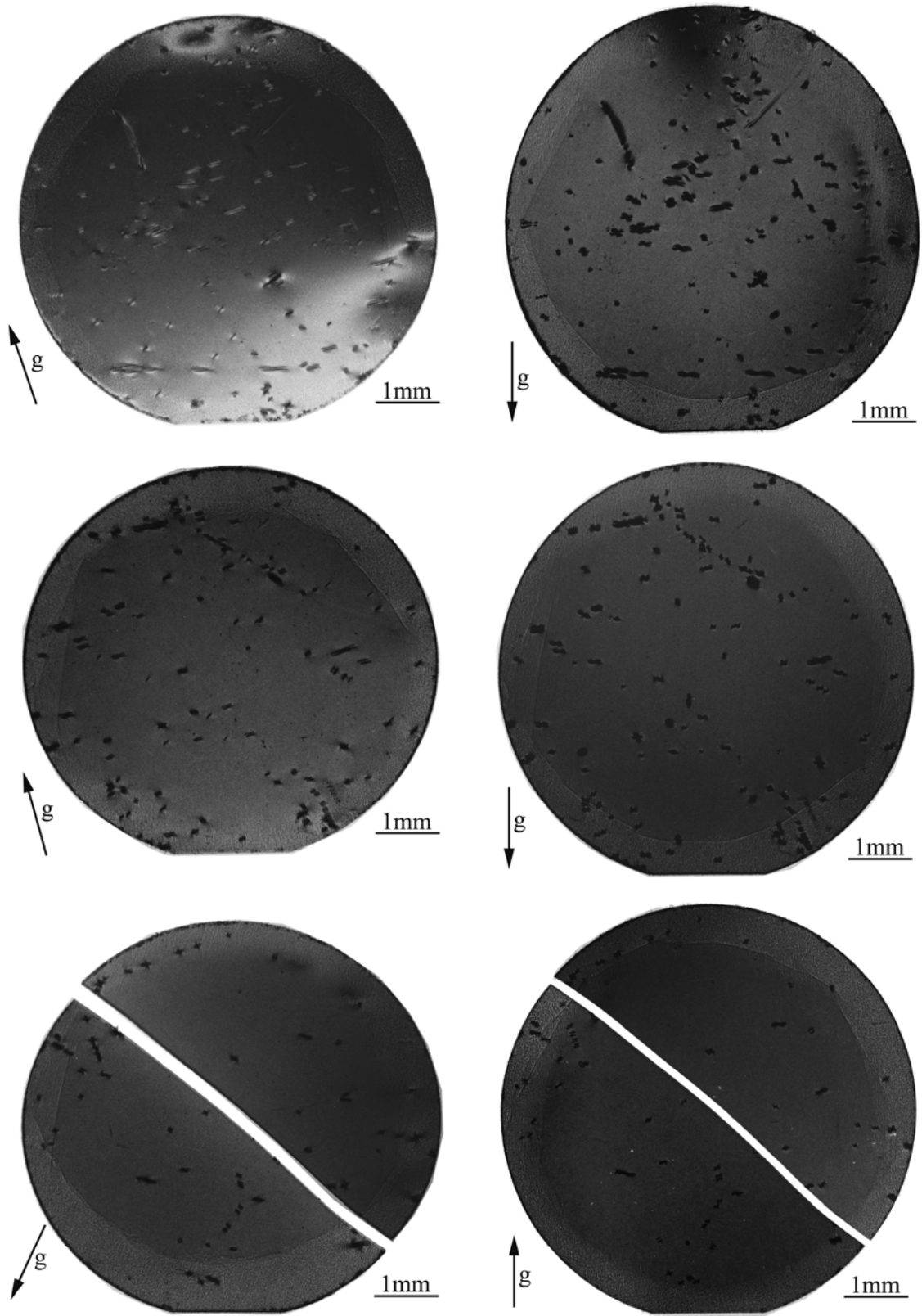


Figure 43. Images recorded from three quartz wafers (batch 2). Wafer 1: images (a)  $g=2-1-10$ , wavelength 1.31 Angstroms and (b)  $g=-1100$ , wavelength 1.31 Angstroms; Wafer

2: images (c)  $g=2-1-10$ , wavelength 1.19 Angstroms and (d)  $g=-2200$ , wavelength 0.76 Angstroms; Wafer 3: images (e)  $g=-2110$ , wavelength 1.19 Angstroms, (f)  $g=2-200$ , wavelength 0.76 Angstroms.

## Study of Quartz Resonators

Total of six quartz resonators, where are with different crystal cuts, different size and different frequency and overtone, were examined by SWBXT using the Stony Brook X-ray Topography Facility at the NSLS, BNL. Transmission diffraction geometry were used to record the images of the resonators.

The ideal procedure would be to examine the quartz crystal at various stages of the manufacturing process, starting with the raw materials (quartz bars) to the processing of the quartz blanks to the finished quartz resonators. Therefore, the initial defect structures and the damages and strains introduced later at various stages of processing could be revealed. Although the study presented here do not cover the whole manufacturing process and the finished resonators were from different sources of quartz crystals other than the one were examined and presented in the previous section, some similar and correlated information can still be revealed due to the wide range of resonators examined and studied.

### *Quartz Resonator A*

Photograph of quartz resonator A are shown in Figure 44. Four transmission topographs with diffraction conditions  $g=\bar{2}50$ ,  $g=\bar{2}30$ ,  $g=\bar{2}55$  and  $g=\bar{2}5\bar{5}$  respectively are shown in Figure 45.

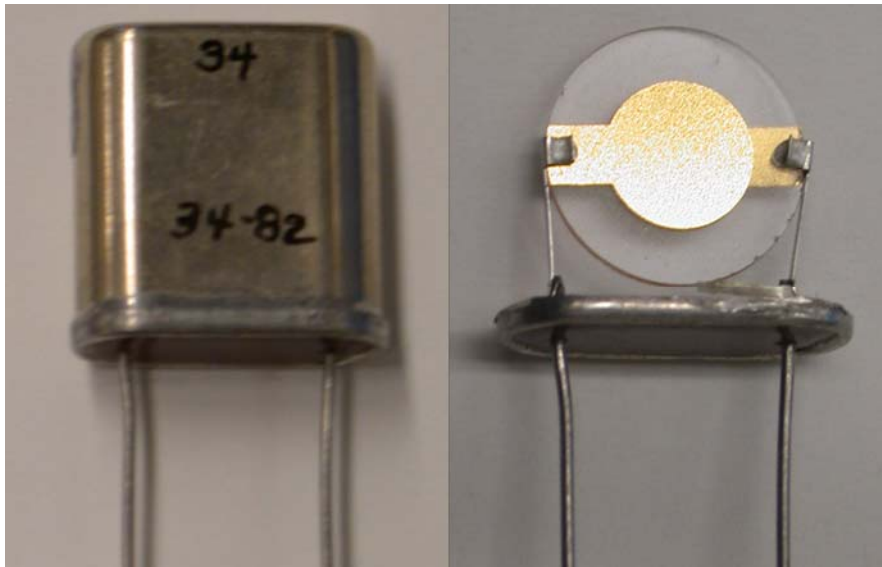


Figure 44. Photographs of quartz resonator A

Some of the features revealed in the topographs are discussed here:

- 1) Lot of straight lines running through in the topographs represents the

dislocations. The black or white contrast observed depends on the diffraction conditions. The line directions of the dislocations vary but tend to be grouped and parallel. High density of dislocations is a major factor to the Q factor of resonators.

- 2) Bonding strain is evident near the pin positions, especially in topographs with  $g = \bar{2}50$  and  $g = \bar{2}30$ . The differences of bonding strains in different diffraction conditions indicate that those strains are presented only along certain directions. It also appears to be localized and relatively short ranges comparing to the dislocations.

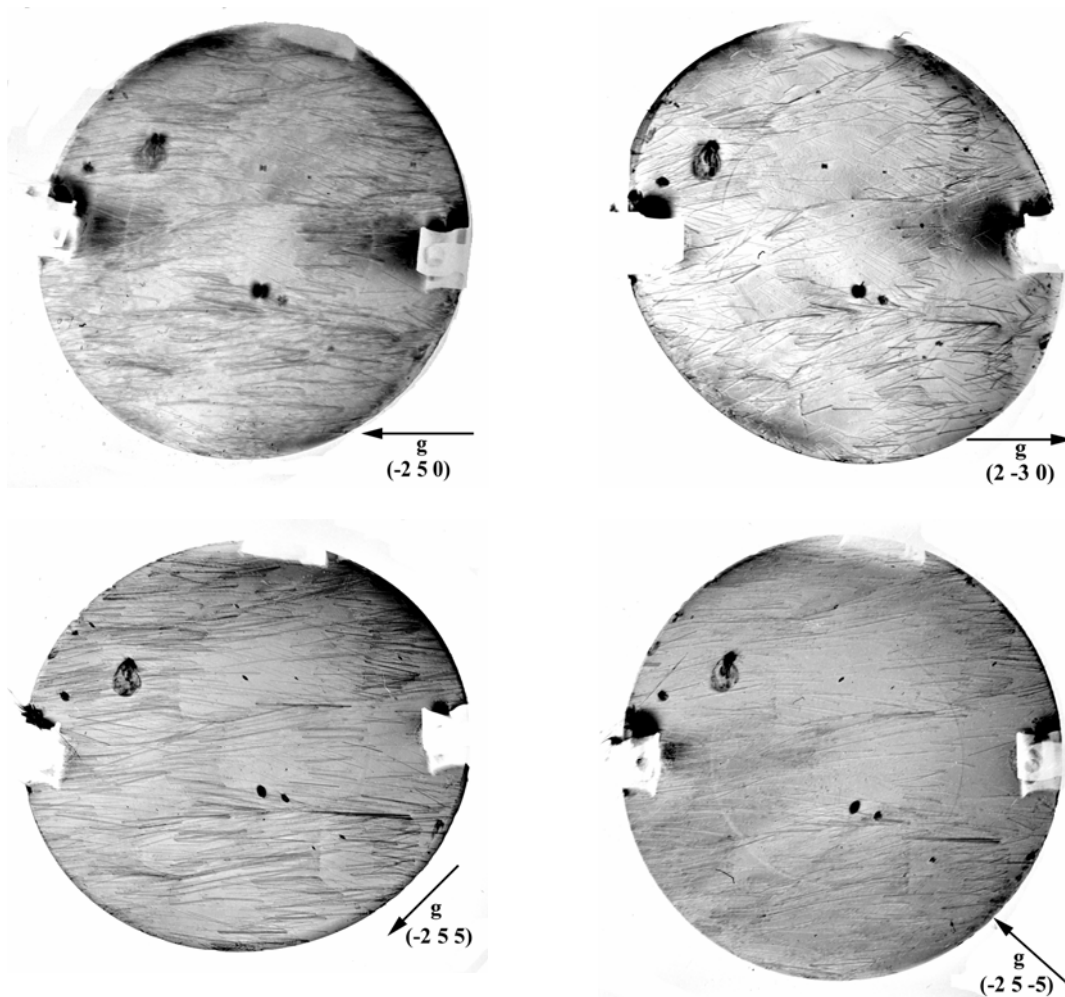


Figure 45. Transmission topographs of quartz resonator A

- 3) Existence of tiny black dots, resembling inclusions can be discerned. These inclusions tend to segregate at certain areas which are clearly separated by boundaries from relatively clear areas which are inclusion free.
- 4) Several black subgrain features are presented in the topographs. They are similar to the subgrains discovered in the quartz bar in previous section and possibly have the same origin.

- 5) Gold thin film electrodes deposited on both sides of the quartz blank surfaces at high temperatures can create stress, which can potentially affect the frequency stability of resonators. The strain at the edge of electrode is presented in all topographs except the one with  $g=\bar{2}55$  diffraction condition. The sign and direction of the strain can be determined by  $\mathbf{g} \cdot \mathbf{u} = 0$  analysis, where  $\mathbf{u}$  is the displacement vector. The results show that  $\mathbf{u}$  is perpendicular to the electrode film edge, so there is no shear stress detected. From the different contrast (black and white) at the different segments of the electrode edge, it can be inferred that the strain in the quartz blank is compressive while the strain in the electrodes is tensile. It is consistent with the fact of the differences in the thermal expansion coefficient between quartz and gold.

### ***Quartz Resonator B***

Photograph of quartz resonator B are shown in Figure 46. Four transmission topographs with diffraction conditions  $g=\bar{5}34$ ,  $g=\bar{5}35$ ,  $g=\bar{7}55$  and  $g=4\bar{1}7$  respectively are shown in Figure 47.



Figure 46. Photographs of quartz resonator B

Some of the features revealed in the topographs are discussed here:

- 1) Long straight lines representing dislocations run parallel through the whole quartz blank. This appears to be consistent with the observation of twin subgrains in the quartz bar presenting in previous section. The black or white contrast of the dislocations is determined by the diffraction conditions of each topograph. The density of dislocation is much lower than that of the quartz resonator A.
- 2) Bonding strain is not clearly presents in the topographs. It is indicative of an inconsistency in the manufacturing process of resonators compared with resonator A.

- 3) Surface dominant contrast associated with the interaction between quartz sample surface and the electrode can be observed in all images. Strain contrast associated with the edge of the electrode superimposed on the contrast associated with the intersecting dislocations.
- 4) Scratches are visible in the center region of the resonator.
- 5) Existence of tiny black dots, resembling inclusions distribute throughout the whole quartz blank. These inclusions also tend to segregate at certain areas, but the separation of inclusion rich and “clear” areas are not as clear as that of resonator A.
- 6) No black subgrain features are presented in all of the topographs.

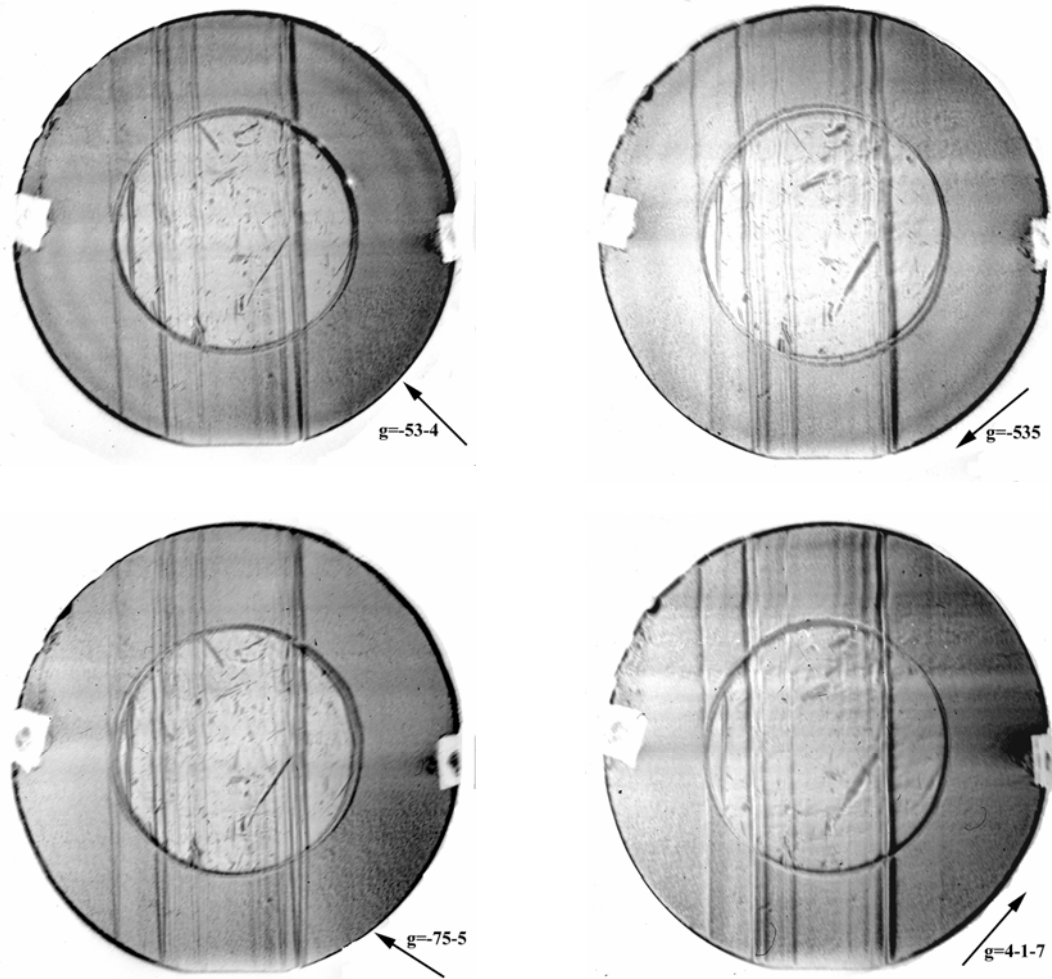


Figure 14. Transmission topographs of quartz resonator B

### ***Quartz Resonator C***

Photograph of quartz resonator C and two transmission topographs are shown in Figure 48.

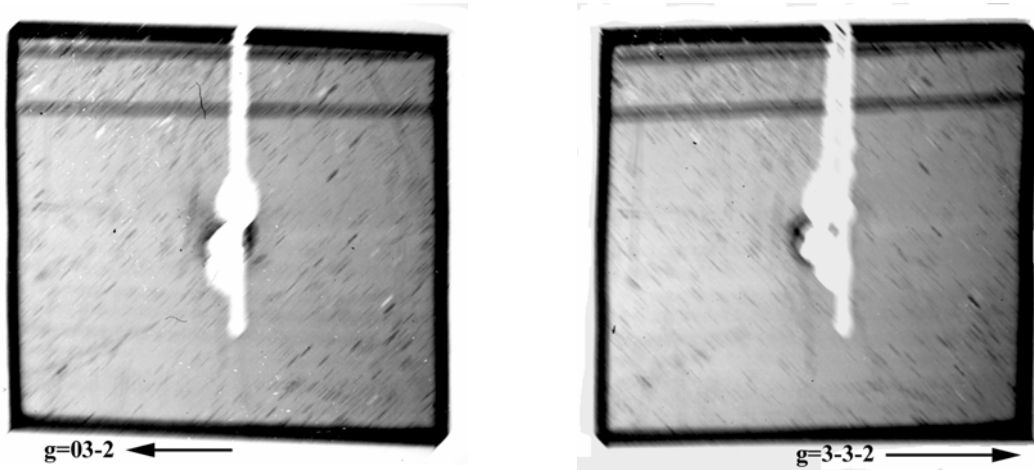


Figure 48. Photographs and transmission topographs of quartz resonator C

Due to the very poor surface finish of the crystal, all the topographs are blur and not much information can be obtained from those images. Only some scratches and some “beat-like” short contrast representing dislocations can be discerned. Bonding strain presents at the pin position in the center of the crystal and no electrode strain presents.

### ***Quartz Resonator D***

Photograph of quartz resonator D are shown in Figure 49. Four transmission topographs with diffraction conditions  $g=03\bar{2}$ ,  $g=\bar{1}0\bar{2}$ ,  $g=30\bar{4}$  and  $g=33\bar{2}$  respectively are shown in Figure 50.

Some of the features revealed in the topographs are discussed here:

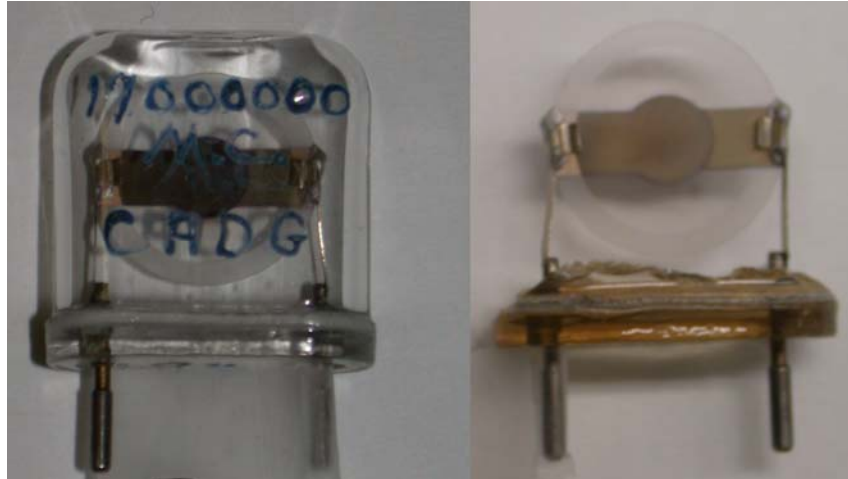


Figure 49. Photographs of quartz resonator D

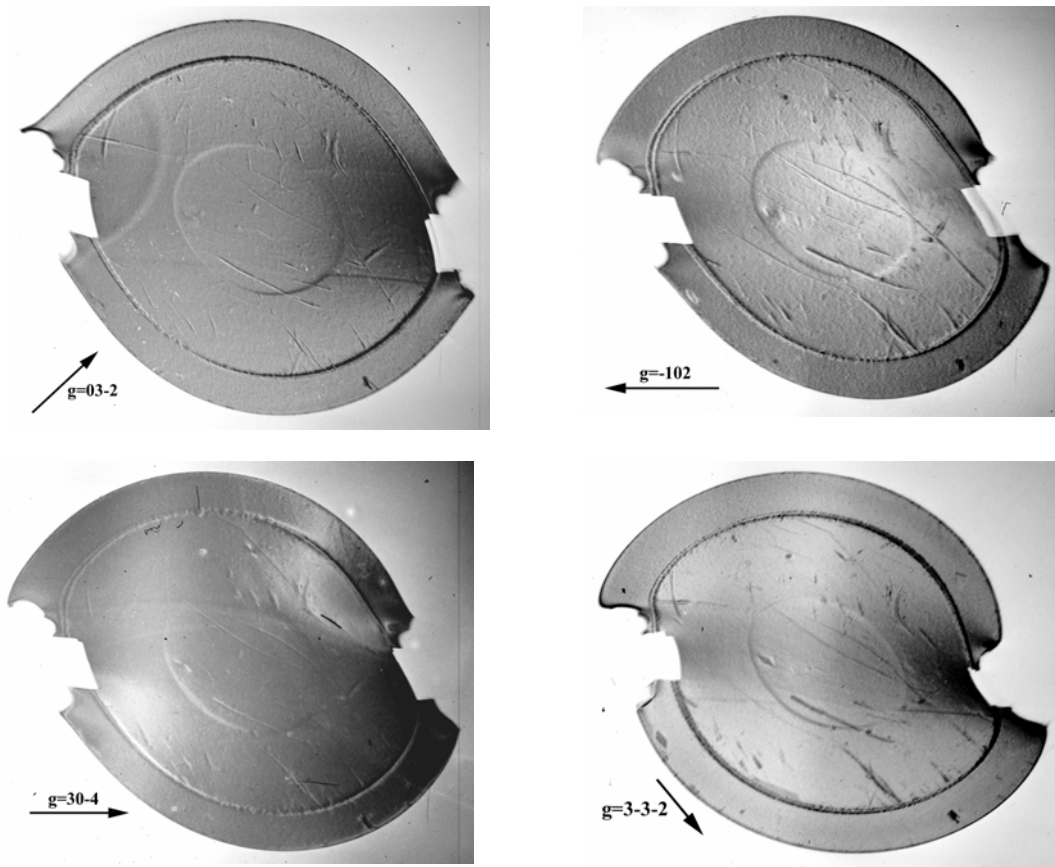


Figure 15. Transmission topographs of quartz resonator D

- 1) Dislocation contrasts are clear in the topographs. The directions of the dislocations vary and have no indication of any preferred direction or directions. All dislocations are short and more localized than resonator A and B. The density of dislocation is much less, too.

- 2) Bonding strain around left pin area is more severe than that around right pin area. It is also indicative of an inconsistency in the manufacturing process of the resonator.
- 3) Scratches are visible in the resonator.
- 4) Surface dominant contrast associated with the interaction between quartz sample surface and the electrode and the material deposited on the edge of the resonator can be observed in all images. Strain contrast associated with the edge of the electrode superimposed on the contrast associated with the intersecting dislocations.
- 5) Tiny black dots contrast of precipitates or inclusions evenly distribute throughout the whole quartz blank. No segregation can be discerned.

### ***Quartz Resonator E***

Photograph of quartz resonator E are shown in Figure 51. Four transmission topographs with diffraction conditions  $g=\bar{1}3\bar{1}$ ,  $g=\bar{1}5\bar{2}$ ,  $g=\bar{1}\bar{1}\bar{2}$  and  $g=\bar{1}3\bar{3}$  respectively are shown in Figure 52.



Figure 51. Photographs of quartz resonator E

Some of the features revealed in the topographs are discussed here:

- 1) The whole quartz crystal is divided into four domains with different orientations.
- 2) Brazil twin boundaries (with clear fault fringe, especially in  $g=\bar{1}3\bar{1}$  diffraction) are dominant features in all topographs. The quartz crystal was optically twinned with both left-handed and right-handed form material mixed in the same quartz crystal. With both electric and optic axes reversed, the overall piezoelectric effect is greatly reduced and the crystal is not suitable for resonator application.

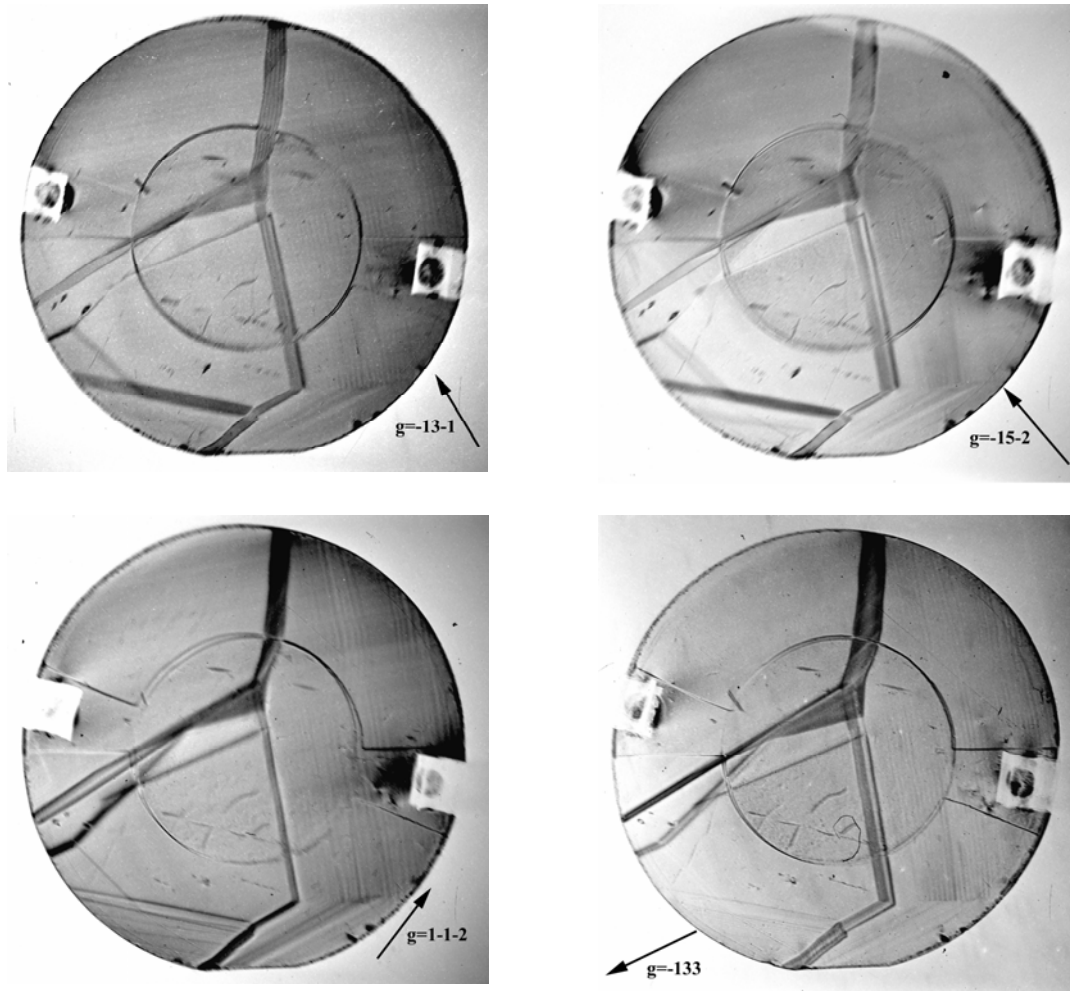


Figure 52. Transmission topographs of quartz resonator E

- 3) Growth striations are also clearly presented in the topographs, especially in the right half of the crystal. They are running along the twin boundaries. And they also outline the two growth sectors which indicates that the growth was occurred on r and z faces.
- 4) Several dislocations are visible in the topographs. This resonator has the lowest dislocation density among all the quartz resonators examined.
- 5) Bonding strain is presented in the surrounding area of the both pins. It is very localized and in a very short range
- 6) Surface dominant contrast associated with the interaction between quartz sample surface and the electrode can be observed in all images. Strain contrast associated with the edge of the electrode superimposed on the contrast associated with the intersecting striations and domain boundaries.
- 7) Scratches are visible in the center region of the resonator.

### *Quartz Resonator F*

Photograph of quartz resonator F are shown in Figure 53. Four transmission topographs with diffraction conditions  $g=\bar{4}71$ ,  $g=\bar{5}11$  and  $g=331$  respectively are shown in Figure 54.



Figure 53. Photographs of quartz resonator F

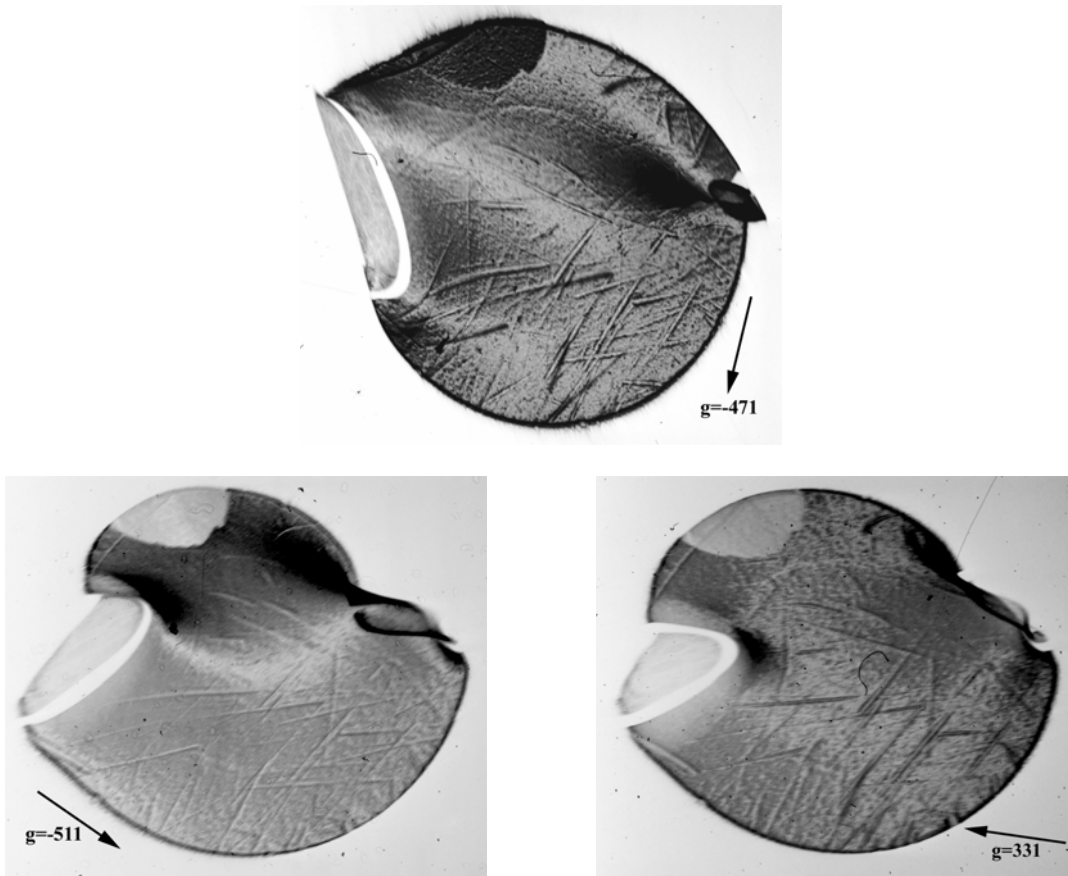


Figure 54. Transmission topographs of quartz resonator F

Some of the features revealed in the topographs are discussed here:

- 1) Due to the very small size of the resonator, the pins and bonding area covers a very high proportion of the crystal surface. The bonding strain is the most significant feature presented here in the topographs. It also would be one of the most important factors of determining the performance of the resonator.
- 2) High density of dislocations is within the crystal with various directions running cross the resonator.
- 3) Evenly distributed precipitates also have a significant presence in the crystal.
- 4) The electrodes cover more than half of the surface of the crystal. Very weak contrast of the edge of electrode present in the topographs, which indicates that the strain introduced by the electrodes is possibly penetrated into the whole crystal.

### **Discussion of the Quartz Crystal Studies**

Here are some remarks about the study of the quartz bars, quartz crystals and the wide range of quartz resonators presented in this report:

- 1) Dislocations are the common defect in the quartz crystals. The presence of clutters of dislocations running along the X direction across the whole crystal is confirmed by the study of quartz bar and quartz resonators;
- 2) Quartz bars should be routinely screened before being put into devices production process to prevent the dislocations in the bar to be transformed into the final product;
- 3) Strains introduced by bonding of the pins are very common defects in the quartz crystals, it with greatly affect the frequency stability of the resonator;
- 4) Strains introduced by the deposition of electrode thin films are also very common to the resonators, and would affect the performance of the device;
- 5) From the different contrast observed (black or white) at the different segments of the electrode edge, it can be inferred that the strain in the quartz blank is compressive while the strain in the film is tensile;
- 6) Extra effort should be put into the production process to minimize the possible strain introduced by bonding of pins and deposition of electrode thin films;
- 7) To reduce the precipitates and inclusions in the quartz crystal, a thorough and complete sweeping process is necessary, and it may have a detrimental effect on the resonator performance.

## **Silicon Carbide**

The goal of the work done at Stony Brook University is to achieve improved understanding of the factors controlling defect replication and modification during the homo-epitaxial CVD growth of 4H-SiC by plan-view and cross-section synchrotron white beam X-ray topography (SWBXT).

Stony Brook University team, led by Prof. Michael Dudley, has focused mainly on the following tasks in the Army Research Lab project:

- **Plan-view SWBXT study of replication/dissociation of MPs after epilayer growth;**
- **Computer modeling of the SWBXT images of dissociated MP;**
- **Cross-sectional SWBXT study of replication/modification of MPs after epitaxial growth;**
- **TEM study of MP dissociation after n<sup>-</sup> drift layer growth.**

### **Plan-view SWBXT study of replication/dissociation of MPs after epilayer growth**

Generally, plan-view SWBXT shows that some MPs are modified, perhaps dissociated, during epitaxial growth. Optical microscopy shows that some hollow cores close after epi-growth. Specific cases were studied in both plan-view and cross-section but detailed changes were obscured by the presence of LAGBs. The observation of the dissociation is complicated because the dissociated TSDs are close to each other and their strain fields overlap. Detailed image simulation has been done to facilitate observation of the dissociation process.

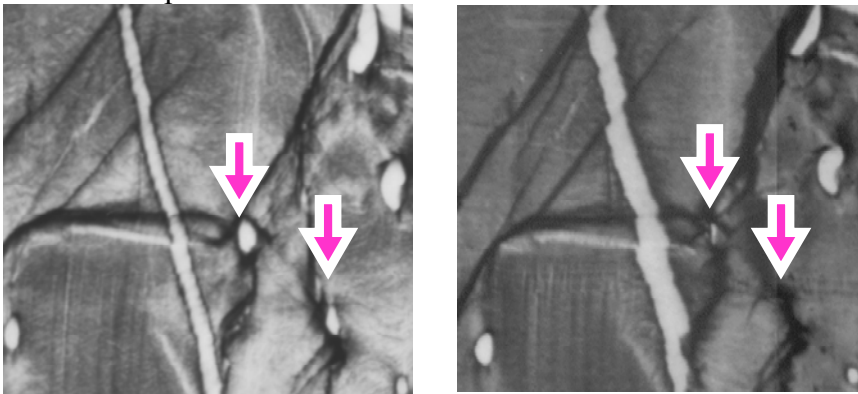


Figure 55. Comparison of (11-28) grazing-incidence SWBXT image before (left) and after (right) epilayer growth. The MPs are clearly modified.

## Cross-sectional SWBXT study of CVD grown epitaxial layers

Cross-sectional transmission SWBXT has been done to study the replication/modification of threading dislocations after epitaxial growth. The conversion from BPDs to TEDs is studied. A cross-sectional SWBXT is shown below. Interface between PVT substrate and CVD grown epilayer can be clearly visualized in the cross-sectional SWBXT image. At the interface, the BPDs which lie on the basal plane are mostly converted into TEDs, which are aligned at some angle to the  $c$ -axis. This conversion is favored due to the image force. In the meantime, the conversion reduces the strain energy because the total strain energy is proportional to the length of the dislocation line, according to Frank's theory. It should be noted that the converted TEDs are not aligning along the  $c$ -axis, but at some oblique angle to it. Further study is going on to address such phenomenon.

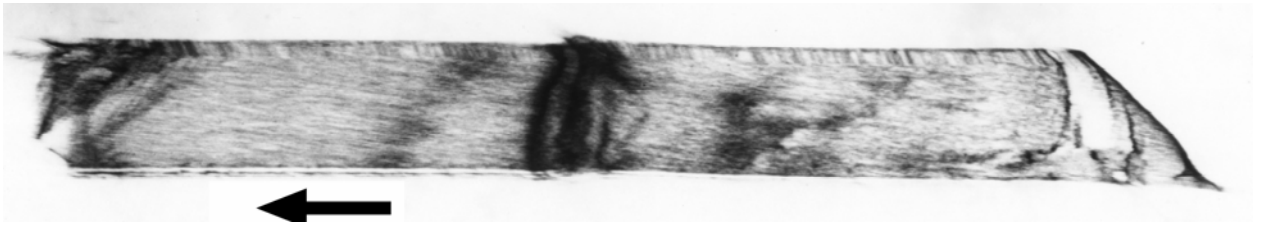


Figure 56. Cross sectional SWBXT of SiC wafer after epilayer growth showing the conversion of BPDs into TEDs during CVD growth. The total thickness is  $\sim 430\mu\text{m}$ .

By comparing the KOH etch pattern between the etch pattern before and after CVD growth, some of the MPs were found to dissociate into etch pit cluster. MPs probably are dissociated into closed-core MPs, although plan-view grazing-incidence SWBXT does not show significant change before and after CVD growth. This is to be discussed in the following section using computer modeling. Optical microscopic images of cross-sectional samples also verify that some hollow cores are close after epitaxial growth at the substrate-epilayer interface. Specific cases were studied (see image below) in both plan-view and cross-section but detailed changes were obscured by the presence of low angle grain boundaries (LAGBs). The observation of the dissociation is complicated because the dissociated TSDs are close to each other and their strain fields overlap. The interference of the contrast from LAGB near the MP prevents from visualizing the dissociation of MP in detail. Improved selection of examples would help this investigation.

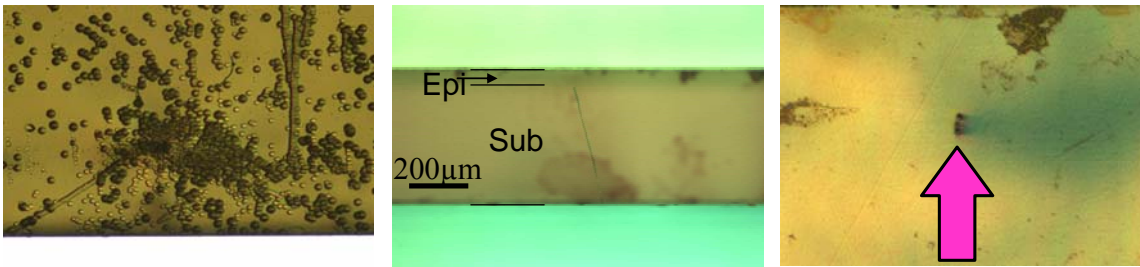


Figure 57. Optical images showing the dissociation of MPs into closed-core TSDs. Left: KOH etch pattern on the epilayer surface; middle: cross sectional view of closing of MP

at the substrate-epilayer interface; right: MP from the back side (C-face) of the wafer.

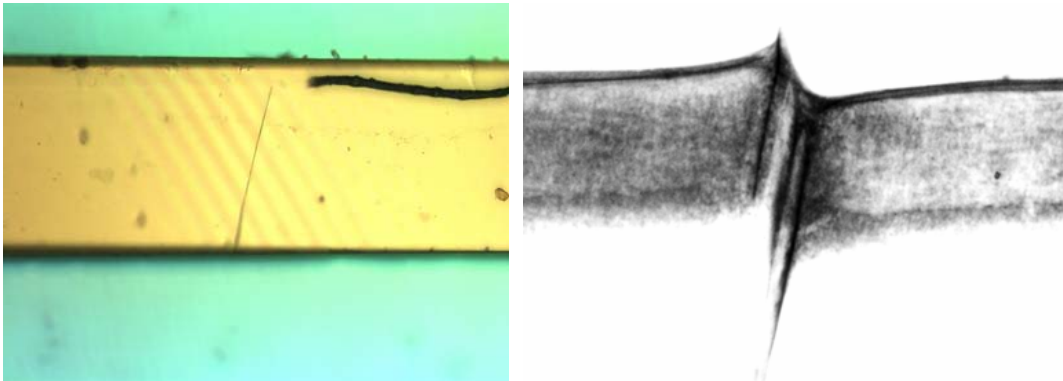


Figure 58. Cross-sectional image showing the closing of MP at the interface between substrate and epilayer (left) and its (0004) transmission SWBXT (right). Sample thickness:  $\sim 430\mu\text{m}$ .

### Computer modeling of the SWBXT images of MP after dissociation into 1c TSD cluster

“Ray-tracing” method has been used to simulate the image of MP before and after dissociation in grazing-incidence SWBXT. The grazing-incidence SWBXT images of MPs have been simulated to be white oval shape with arcs of dark contrast at the end of the long axis. When a MP with Burgers vector  $nc$  is dissociated into  $n$  number of elementary TSDs which are close with other, the total displacement fields, which are the combination of all the TSDs, contribute to the SWBXT image. Simulated image indicates although SWBXT does not show significant change of MP images, it does not necessarily mean that the MPs are not dissociated. The overlapping of the strain fields of independent elementary TSDs results in the similarity of their SWBXT images.

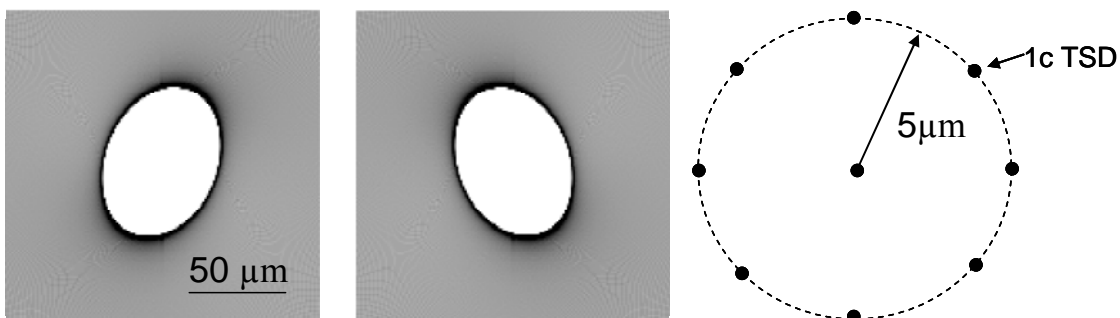


Figure 59. Ray-tracing simulated images of dissociated 1c TSD cluster. The simulated image elementary TSD cluster which consists of  $n$  number of 1c TSDs appears as the same configuration as a MP with Burgers vector  $nc$ .

## TEM study of MP dissociation after n<sup>-</sup> drift layer growth

Plan-view TEM is going on to study the dissociated MPs. Specimen was polished from substrate side and ion milled. The etch pit cluster was taken as a reference. No hollow core was observed after the substrate was polished away. Closed-core TSDs were observed in the etch pit cluster, which are probably dissociated from MP. At high magnification, the TSD is observed to run through the whole sample. TEM results show that the MP has dissociated into closed-core TSDs.

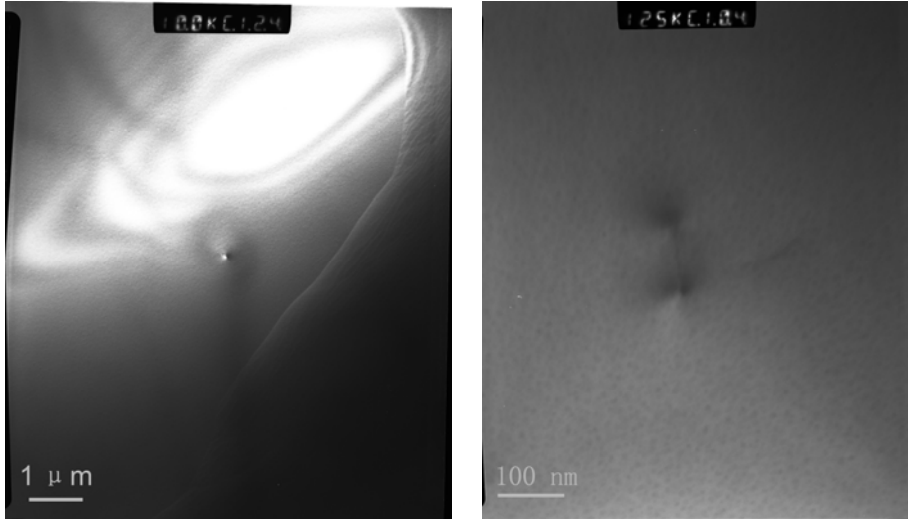


Figure 60. (1-100) dark field image of a closed-core TSD present in the etch pit (left). It is probably dissociated from the MP during CVD growth. Multibeam image at higher magnification (right), showing the tilted TSD running through the sample.

In summary, plan-view and cross-section SWBXT have been used to study the replication/modification of MPs during homo-epitaxial CVD growth of 4H-SiC. Some MPs are clearly modified in the plan-view SWBXT images. Some of the MPs do not show clear change in the plan-view SWBXT images. However, it does not necessarily mean that they are not dissociated, since simulation indicates that the image of TSD cluster appears similarly to a MP, the Burgers vector of which is the sum of the TSDs. On the other hand, optical images of cross-sectional samples clearly show that the hollow cores are closed at the substrate-epilayer interface. Specific cross-sectional samples were studied using transmission SWBXT but detailed changes were obscured by the presence of low angle grain boundaries (LAGBs). The interference of the contrast from LAGB near the MP prevents from visualizing the dissociation of MP in detail. Improved selection of examples would help this investigation. Plan-view TEM studies indicate that some MPs have dissociated into closed-core TSDs.